Astronomy & Astrophysics manuscript no. main
April 20, 2021

Constraining AGN duty cycle in the cool-core cluster MS 0735.6+7421 with LOFAR data

Nadia Biava[1,2], Marisa Brienza[1,3], Annalisa Bonafede[1,3], Myriam Gitti[1,3], Etienne Bonnassieux[1,3], Jeremy Harwood[4], Alastair C. Edge[5], Christopher J. Riseley[1,3], and Adrian Vantyghem[6]

[1] Dipartimento di Fisica e Astronomia, Università di Bologna, via P. Gobetti 93/2, I-40129, Bologna, Italy
[2] INAF - Osservatorio di Astrofisica e Scienza dello Spazio di Bologna, via Gobetti 93/3, I-40129 Bologna, Italy
[3] INAF - Istituto di Radioastronomia, Bologna Via Gobetti 101, I-40129 Bologna, Italy
[4] Centre for Astrophysics Research, University of Hertfordshire, College Lane, Hatfield AL10 9AB, UK
[5] Centre for Extragalactic Astronomy, Durham University, DURHAM, DH1 3LE, UK
[6] University of Manitoba, Department of Physics and Astronomy, Winnipeg, MB R3T 2N2, Canada

Received ; accepted

ABSTRACT

Context. MS 0735.6+7421 is a galaxy cluster which hosts a central radio galaxy with a very steep spectrum, produced by one of the most powerful known jetted active galactic nuclei (AGN). The radio plasma, ejected at nearly light speed from the central AGN, have displaced the intra-cluster medium, leaving two pairs of cavities observable in the X-ray, associated to two different outbursts, and have distributed energy to the surrounding medium. While the age of the cavities has previously been estimated from the X-rays, no confirmation from the radio data is available. Furthermore, to-date the radio spectrum has only been derived from integrated flux density measurements, without providing the spatial distribution which could help us to understand the nature of this source.
Aims. The aim of this work is to perform for the first time a detailed, high-resolution spectral study of the source at radio frequencies and investigate its duty cycle to be compared with previous X-ray estimates.
Methods. We use new observations at 144 MHz produced with the LOw Frequency ARray (LOFAR) together with archival data at higher frequencies (235, 325, 610, 1400 and 8500 MHz), to investigate the spectral properties of the source, and we use radiative models to constrain the age of the source.
Results. At LOFAR frequency, the source presents two large outer radio lobes, wider than at higher frequencies, and a smaller Intermediate lobe located south-west of the core. A new inspection of X-ray data, allowed us to identify an intermediate cavity, associated with that lobe, indicating the presence of a further phase of jet activity. The radio lobes have a steep spectrum even at LOFAR frequencies, reaching $\alpha_{144}^{610} = 2.9$ in the outer lobes and $\alpha_{144}^{610} = 2.1$ in the Intermediate lobe. Fitting the lobe spectra using a single injection model of particle ageing, we derived a total age of the source between 170 and 106 Myr, in agreement with the buoyancy and sound crossing time-scales derived from X-ray data. Thanks to the resolution of the spectral age map we performed, we are able to reconstruct the duty cycle of the source. There were three phases of jet activity, with the AGN being active for most of the time with only brief quiescent phases, ensuring the repeated heating of the central gas. Finally, we estimated the minimum energy inside the outer lobes, finding that a source of additional pressure support must be present to sustain the bubbles against the pressure of the external medium.

Key words. radio continuum: galaxies - galaxies: jets - galaxies: clusters: individual: MS0735.6+7421

1. Introduction

Galaxy clusters are the largest gravitationally-bound objects in the Universe, with masses up to $\sim 10^{15}$ $M_\odot$, hosting hundreds to thousands of galaxies. The space in between the galaxies is filled with a hot ($T \sim 10^7 - 10^8$ K) and rarefied gas (electron density $n_e \sim 10^{-3}$ cm^{-3}), known as the intra-cluster medium (ICM), which emits in the X-ray band through bremsstrahlung radiation (e.g. Mitchell et al. 1976; Serlemitsos et al. 1977; Forman & Jones 1982). Radio observations reveal the presence of relativistic particles and magnetic field in the ICM (see e.g. review by van Weeren et al. 2019).

Galaxy clusters often host active galactic nuclei (AGN) with jets of relativistic plasma, which emit synchrotron radiation and are mostly visible at radio frequencies (e.g. De Young 1984; de Young 2002; Tadhunter 2016). The sizes of these sources range from a few kpc to a few Mpc, extending well beyond the host galaxy.

The hot X-ray emitting gas in the central region of many cool-core clusters has a radiative cooling time that is much shorter than the Hubble time. Therefore, a cooling flow is expected to develop (Fabian 1994). In the standard model of cooling flows, the gas cools from the cluster temperature down to temperatures significantly below 1 keV, emitting different atomic lines. However, high-resolution spectroscopic observations with the *Chandra* and XMM-*Newton* X-ray telescopes have not found evidence of the predicted cooling to low temperatures, implying that some source of heating must balance the radiative losses (Peterson et al. 2003; Peterson & Fabian 2006).

The most plausible heating mechanism is mechanical feedback from the AGN hosted by the cluster — in particular, by the brightest cluster galaxy (BCG; see e.g. reviews by McNamara & Nulsen 2007, 2012; Hardcastle & Croston 2020). Evidence of this hypothesis is found in the X-ray cavities observed in a number clusters, on scales approximately coincident with the lobes of the central radio galaxy (e.g. McNamara et al. 2000; Fabian

et al. 2000). In this scenario, the radio plasma emitted by the central AGN displaces the X-ray emitting gas, creating a low-density bubble, which rises buoyantly and expands, distributing energy to the surrounding medium. To suppress cooling over the age of clusters, repeated events of AGN jet activity are required to occur on time-scales shorter than the cooling time.

Indeed, in some objects two systems of cavities have been observed (e.g. Nulsen et al. 2005; Wise et al. 2007; Vantyghem et al. 2014) or the AGN shows multiple radio lobes related to repeated outbursts (Morganti 2017), sometimes pointing in different directions (e.g. RBS797; Doria et al. 2012; Gitti et al. 2006). For restarted sources, the spectral properties of the radio plasma can be used to derive their duty cycle, that is the fraction of time during which the AGN is active (e.g. Harwood et al. 2013, 2015; Brienza et al. 2020).

However, performing resolved spectral studies to derive accurate estimates of the age of the AGN plasma is not trivial, as it requires high resolution and sensitive radio observations over a wide range of frequencies. The advent of instruments such as the LOw Frequency ARray (LOFAR; van Haarlem et al. 2013) allows, for the first time, to perform these studies at low frequencies.

1.1. MS 0735.6+7421

One of the most famous examples of AGN mechanical feedback is represented by the radio source located at the center of the cool-core galaxy cluster MS 0735.6+7421 (hereafter MS0735). The source (RA = 07:41:40.3, DEC = +74:14:58.0) has a redshift of $z = 0.216$, corresponding to a scale of $1'' = 3.53$ kpc (assuming a ΛCDM cosmological model with $\Omega_\Lambda = 0.7$, $\Omega_m = 0.3$ and $H_0 = 70$ km s^{-1} Mpc^{-1}).

This cluster was first identified as a cooling flow candidate by Donahue et al. (1992) and then confirmed by Donahue & Stocke (1995). Thanks to Very Large Array (VLA) data, the central radio source (4C +74.13) was identified as a radio galaxy with a clearly defined core and outer lobes (Cohen et al. 2005). They also found a significant extension of the central emission towards south-west, which may be the result of the jet interacting with the ICM, or an inner lobe generated by a more recent radio outburst. Using VLA data at 325 MHz and 1425 MHz, with a resolution of $21''$, they found steep spectra in all the main features of the source: $\alpha_{325}^{1425} = 1.54 \pm 0.04$, for the central region and $\alpha_{325}^{1425} = 3.17 \pm 0.05$ and $\alpha_{325}^{1425} = 3.13 \pm 0.05$ for the northern and southern outer lobes, respectively (where $S_\nu \propto \nu^{-\alpha}$).

Chandra X-ray observations revealed the presence of two giant cavities, each roughly 200 kpc in diameter, and a shock front surrounding them (McNamara et al. 2005). The radio lobes partially fill the cavities, suggesting that the gas was displaced and compressed by the advancing radio jets. The total energy involved in the process is $\sim 6 \times 10^{61}$ erg, making this one of the most powerful known outbursts, together with the Ophiuchus galaxy cluster (Giacintucci et al. 2020). The total energy is enough to quench the cooling flow and to heat the gas within 1 Mpc by ~ 0.25 keV per particle. *XMM* data confirmed these results and showed that most cooling flow clusters are likely experiencing such powerful outbursts during episodes lasting for a small fraction ($\sim 10\%$) of their age (Gitti et al. 2007).

Using deep *Chandra* observation Vantyghem et al. (2014) detected a second pair of cavities located along the radio jets in the inner 20 kpc, corroborating the hypothesis of a renewed period of AGN activity. They estimated the cavity ages using the buoyancy, sound crossing, and refill time-scales. The mean ages of the northern and southern outer cavities are 150 Myr and 170 Myr, respectively, while the age of the surrounding shock front (110 Myr) which should be comparable to the true cavity age, is shorter than the mean rise time. So the cavity ages are slightly overestimated while the power to inflate the bubbles (for the northern cavity, 9×10^{45} erg s^{-1}; for the southern cavity, 8×10^{45} erg s^{-1}) is underestimated. For the inner cavities, they found a mean age of 48 Myr (northern) and 42 Myr (southern). The power of these cavities (northern 2.8×10^{44} erg s^{-1} and southern 2.4×10^{44} erg s^{-1}) is 30 times smaller than the outer cavity power, implying that the jet power has varied significantly over time (Vantyghem et al. 2014). The outburst interval, estimated as the difference between the ages of the outer and inner cavities, is 110 Myr. It is shorter than the central cooling time, preventing the majority of the surrounding gas from cooling. Repeated heating of the central gas supplies enough energy to prevent cooling, and may explain the lack of star formation in the system (McNamara et al. 2009).

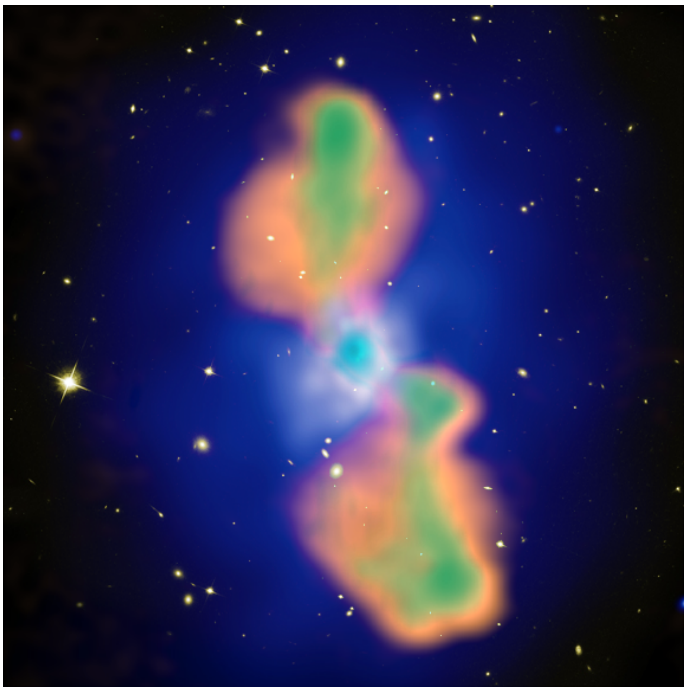

Fig. 1: Composite image of MS0735, obtained combining the *Chandra* X-ray image (blue), the I-band image taken by the Hubble Space Telescope (white), the radio wavelengths observed with LOFAR at 144 MHz (orange) and observed with the VLA at 325 MHz (green). The LOFAR lobes are wider than at 325 MHz and they perfectly fills the cavities.

However, the ages derived from the cavity rise time are approximate and are an indirect probe of the AGN duty cycle. A first estimate of the radiative age of the lobes from radio data was performed by Bîrzan et al. (2008). Based on integrated spectral analysis of VLA data at 235 MHz and 1400 MHz, they estimated a synchrotron age of 97 Myr, which reduces to 50 Myr if adiabatic losses are considered.

Integrated models of spectral ageing have long been used to determine the age of radio galaxies. However they provide a poor, frequency dependent description of a source's spectrum, compared to recent well resolved studies that use modern analysis techniques on small spatial scales (Harwood 2017a).

In this paper, we present new radio observations of MS0735, performed with LOFAR at 144 MHz. A composite image of the

source, created with our new LOFAR data together with archival VLA 325 MHz data, is shown in Fig. 1. Thanks to the high resolution and sensitivity provided by LOFAR at 144 MHz, we can characterize the morphology, spectral properties, and radiative age of this source in detail for the first time. Our aim is to perform a resolved spectral study of MS0735, combining LOFAR data with archival observations at higher frequencies, to investigate the duty cycle of the central AGN and its energetics.

We note that LOFAR snapshot observations of MS0735 has already been shown by Kokotanekov et al. (2017). This observation was performed during the first LOFAR all-sky survey, the Multifrequency Snapshot Sky Survey (MSSS; see Heald et al. 2015). The MSSS image of MS0735 has a resolution of 27.8″ and a RMS noise of 30 mJy beam^{-1} at 140 MHz, neither of which is sufficient for a resolved spectral study.

The paper is organised as follows: in Sect. 2 we describe the data used in our study and their reduction techniques; in Sect. 3, we present our results and we discuss them in Sect. 4, while our conclusions are reported in Sect. 5. Throughout the paper the spectral index, α, is defined using the convention $S \propto \nu^{-\alpha}$.

2. Data

To investigate the spectral properties and estimate the radiative age of the radio lobes of MS0735, we use new 144 MHz LOFAR data together with archival data from the VLA and the Giant Metrewave Radio Telescope (GMRT; Swarup 1990), covering the frequency range 144−8460 MHz.

We have reprocessed archival observations performed with the VLA at 325, 1420 and 8460 MHz and the GMRT at 235 and 610 MHz. In the following sections, we describe these observations and the data reduction procedures. A summary of the radio observational details is reported in Table 1. We present the final images across our frequency range in Figs. 2 and 3. Their properties are listed in Table 2.

Finally, we compare the radio morphology of the source with X-ray features, shown in Fig. 4, and the radiative age of the radio lobes with X-ray cavity time-scales, using *Chandra* X-ray observations of this source presented in Vantyghem et al. (2014). We report here only a brief description of these observations.

2.1. LOFAR observation and data reduction

The source was observed on 23 May 2018 using the LOFAR High Band Antennas (HBA) in the `HBA_DUAL_INNER` mode. The target was observed for a total integration time of 8 h, using all the LOFAR stations: core stations, remote stations and international stations. International stations were not used in this work, and were flagged before calibration. The observations were performed using a dual-beam mode setup, co-observing with the LOFAR Two-Metre Sky Survey (LoTSS; Shimwell et al. 2017). We observed in the frequency range 110−190 MHz, divided in 244 sub-bands of 64 channels each, with a sampling time of 1 s. Other details, such as the list of calibrators, are reported in Table 1.

This observation is carried-out in co-observing mode with the LOFAR Surveys Key Science project. Data were calibrated using the direction-independent (DI) pipeline described in Shimwell et al. (2017) and the direction-dependent (DD) pipeline that uses `DDF` and `killMS` (Tasse et al. 2018; Tasse 2014a,b; Smirnov & Tasse 2015), following the same approach used for the LoTSS 2nd data release (Shimwell et al. 2019).

Sources outside 30′ from the target were subtracted using the DD gains found by `killMS`, and the extracted field was then self-calibrated further and imaged, using `DPPP` and `WSclean` (van Diepen et al. 2018; Offringa et al. 2014). The flux density scale was set according to Scaife & Heald (2012), and subsequently verified through comparison with the TIFR GMRT Sky Survey (TGSS, Intema et al. 2017). The flux calibration error is estimated to be 10% (Hardcastle et al. 2020).

2.2. VLA observations and data reduction

MS0735 has previously been observed by the VLA in a number of different bands and configurations. We used the following specific datasets:

- 325 MHz, A-configuration, observed on 24 December 2004. The observation was performed using 26 antennas, for a total time on target of 2.4 h, divided into 4 scans alternated by 2-minute observations of the phase calibrator. The flux density calibrator was observed at the end of the observation for 6 minutes. The frequency band was divided in two spectral windows of 31 channels each, for a total bandwidth of 3 MHz. The data were recorded using a dual-mode polarization.
- 325 MHz, B-configuration, observed on 4 December 2003. The target was observed for 3.6 h divided in 3 scans alternated with 3 minutes of phase calibrator observations. The flux density calibrator was observed at the beginning and end of the observing run. 26 antennas were used. The observing band was divided in two sub-bands with 15 channels each of 391 kHz width for a total bandwidth of 12 MHz.
- 325 MHz, C-configuration, observed on 24 December 2006. The observation was performed using 25 antennas some equipped with the old VLA receivers, whereas the others were done with the new receivers. EVLA-VLA baselines were affected by closure errors. We corrected for this effect using the flux density calibrator. The source was observed in 14 time-scans for a total time of 4 h. The phase calibrator was observed for 2 minutes before every target scan, while the flux density calibrator was observed at the beginning and end of the observing run for 4 minutes each time. The data were recorded using two sub-bands of 31 channels each, for a total bandwidth of 6 MHz.
- 1420 MHz, A-configuration, observed on 24 October 2004. The observation was performed using 26 antennas and two single-channel sub-bands with a width of 25 MHz each. The source was observed for roughly 2h, alternated by 2 minutes observations of the phase calibrator. The flux density calibrator was instead observed at the end of the observation for 3 minutes.
- 1420 MHz, B-configuration, observed on 19 August 2006. Observation performed using 25 antennas, four of which were equipped with the old VLA receivers. The latter were flagged from the dataset because they clearly provided a different response with respect to the upgraded antenna, and no suitable calibrator was observed to correct for this effect. The data were recorded in two single-channel sub-bands with a width of 50 MHz. The source was observed for a total time of 5h divided into 12 minutes time-scans. The flux density calibrator was observed at the beginning and end of the observation (4 minutes each time) while the phase calibrator was observed alternated with the source for 3 minutes every time-scan.
- 1420 MHz, C-configuration, observed on 15 April 2004. Observation performed using 27 antennas, 2 sub-bands of 7 channels each for a total bandwidth of 22 MHz. The data

Table 1: Summary of the observational details.

Telescope	Frequency	Configuration	Target TOS	Calibrators	Observation date
LOFAR	144 MHz	HBA-dual inner	8h	3C196	23 May 2018
GMRT	235 MHz	-	6h	3C147, 3C286, 0834+555	4 December 2009
VLA	325 MHz	A	2.4h	3C286, 0749+743	24 December 2004
VLA	325 MHz	B	3.6h	3C147, 0749+743	4 December 2003
VLA	325 MHz	C	4h	3C286, 3C184	24 December 2006
GMRT	610 MHz	-	6h	3C147, 3C286, 0834+555	4 December 2009
VLA*	1420 MHz	A	2h	3C286, 0749+743	24 October 2004
VLA	1420 MHz	B	5h	3C286, 0954+745	19 August 2006
VLA	1420 MHz	C	3.4h	3C147, 0841+708	15 April 2004
VLA*	8460 MHz	A	1.7h	3C286, 0749+743	17 October 2004
VLA*	8460 MHz	D	4.5h	3C147, 0721+713	28 November 2005

Notes. *Observations considered only for the analysis of the central emission.

Table 2: Image properties.

Telescope	ν [MHz]	uv-range [λ]	Beam size	RMS [mJy beam^{-1}]	Fig.
LOFAR	144	48 ~ 480000	7.0"×4.5"	0.2	2
GMRT	235	30 ~ 19173	20"×12"	2.7	3
VLA	325	37 ~ 40186	7"×5"	0.53	3
GMRT	610	80 ~ 49375	7"×4"	6.0×10^{-2}	3
VLA	1420	157 ~ 54376	10"×10"	4.2×10^{-2}	3
VLA	8460	807 ~ 29186	9"×7"	1.2×10^{-2}	3

were recorded for a total integration time on target of 3.4 h divided into 5 time-scans. The flux density calibrator was observed at the beginning and end of the observing run for a total time of 10 minutes; the phase calibrator was observed for 2 minutes alternating with scans on target.

– 8460 MHz, A-configuration, observed on 17 October 2004. The source was observed for 1.7h using 25 antennas. The data were recorded in two single-channel sub-bands with a width of 25 MHz each. The phase calibrator was observed alternating with the target for 2 minutes each time, while the flux density calibrator was observed at the end of the observation for 2 minutes.
– 8460 MHz, D-configuration, observed on 28 November 2005.
The observation was performed using 23 antennas and 2 single-channel spectral windows centred at 8440 MHz and 8490 MHz with a bandwidth of 50 MHz each. The target was observed for 4.5 h divided in 10 scans interspersed with 2 minutes phase calibrator observations. The flux density calibrator was observed for 8 minutes at the beginning of the run.

All data sets were reduced with Common Astronomy Software Applications (CASA, version 5.4; McMullin et al. 2007) using the following steps: after manual flagging, we performed calibration in the standard manner. The flux density scale was set according to Perley & Butler (2013) for all data sets except for the data at 325 MHz, for which we used the scale of Scaife & Heald (2012). The flux calibration error is estimated to be 5% for P-band and L-band and 2% for X-band (Scaife & Heald 2012; Perley & Butler 2013).

Following standard calibration, we performed several cycles of phase-only and amplitude-and-phase self-calibration at 325 MHz and 1420 MHz. Self-calibration was also attempted at 8460 MHz, but due to the low flux density of the source, the process did not improve the gain solutions and the solutions were not applied. Finally, we combined all individual data sets at matching frequencies (325 MHz, 1420 MHz and 8460 MHz) and jointly deconvolved them to improve the *uv*-coverage.

2.3. GMRT observations and data reduction

The source was observed with the GMRT at 235 MHz and 610 MHz, on 4 December 2009 in dual-frequency mode, using the GMRT Hardware Backend (GHB). In observations performed with GHB, the 32 MHz bandwidth is typically split over an upper-side band (USB) and lower-side band (LSB), both recorded in separate LTA files.

For the data at 235 MHz we were able to calibrate only the USB, due to the lack of good calibrator scans in the LSB. The bandwidth is thus limited to 16 MHz. The target was observed in 9 time-scans for a total integration time of 6 h. The source 3C286 was used as flux-density calibrator and observed at the end of the observing run for 12 minutes.

The flux calibration error is estimated to be 10% (Chandra et al. 2004). We processed the data using the Source Peeling and Atmospheric Modelling (SPAM; Intema 2014; Intema et al. 2017) pipeline that corrects for ionospheric direction dependent effects. The output calibrated visibility data were then imported into CASA for imaging.

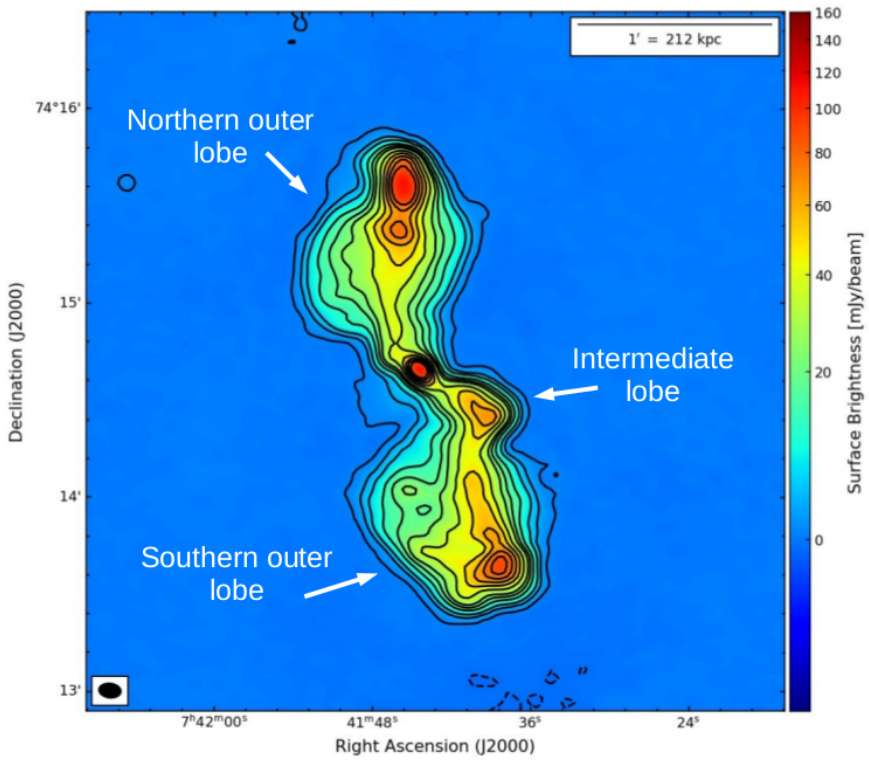

Fig. 2. LOFAR 144 MHz radio map of MS0735 at resolution of 7.0″ × 4.5″. Contour levels: [−1,1,5,10,20,30,40,60,80,100,120,140] × 3σ (where σ = 0.2 mJy beam^{-1}). The beam is shown in the bottom left corner.

2.4. X-ray observations

We used the *Chandra* data already published in Vantyghem et al. (2014) to perform some further analysis as described in Sect. 3.2. The source was observed seven times with *Chandra* in June 2009, for a cumulative exposure time of 477 ks. Each observation was calibrated in the standard way (see Vantyghem et al. 2014, for more details) and then imaged by summing events in the energy range 0.5–7.0 keV. These images were then combined to create a single mosaic image to study the X-ray emission. Point sources were identified and removed. Finally, the best-fitting double-β model was subtracted from the cluster emission, producing the residual image reported in the left and middle panels of Fig. 4.

3. Results

3.1. Radio morphology

In Fig. 1, we show a composite image of MS0735, obtained combining the Hubble Space Telescope I-band image (yellow), the *Chandra* X-ray image (blue) and the radio image at two different frequencies, LOFAR 144 MHz (orange) and VLA 325 MHz (green), at similar resolution of 7"x5", to compare the extension of the radio emission. The radio lobes at LOFAR frequency are clearly wider than previously found with the VLA at higher frequencies and now completely fill the X-ray cavities. In Fig. 2, we show the high-resolution image of MS0735 as seen with the LOFAR-HBA at a central frequency of 144 MHz. The two radio lobes, named northern and southern outer lobes, extend in the north-south direction for ∼ 75″ ≅ 260 kpc from the bright central emission. At the extreme edge of the lobes there is an increase of the surface brightness, which can be interpreted as hotspots.

At this resolution we can clearly see the extended emission south-west of the core, which was previously noted at higher frequencies by Cohen et al. (2005). This was suggested to either be a signature of a second epoch of AGN activity, or a bending of the southern jet direction because of the interaction with the ICM. Our new analysis of the X-ray data, as discussed in Sect. 3.2, points to the presence of a further cavity corresponding to this radio emission, that was not noticed before. This together with the radio morphology observed at high resolution (see LOFAR and VLA images, 2 and 3) supports the idea that this emission represents a radio lobe associated with a further phase of jet activity, occurring between the two already discovered by Vantyghem et al. (2014). It is visible in the central panel of Fig. 4, where the LOFAR contours are superposed on the X-ray image, and the radio emission fills the newly detected cavity, represented with a red ellipse. From here on, we will refer to this emission as to the 'Intermediate lobe'. At its edge there seems to be a hotspot, based on the increase in surface brightness. The bending of this emission with respect to the outer lobes indicates that the reactivated jet has changed its direction. A counterpart of this Intermediate lobe, north-east of the core, is not detected. This could be due to projection effects for instance Doppler boosting (e.g. Blandford & Königl 1979; Orr & Browne 1982; Kellermann & Owen 1988; Hardcastle et al. 1998).

From Vantyghem et al. (2014) we know that a third series of cavities is present in the innermost regions of the source. These are shown in the right panel of Fig. 4 with green ellipses, where the soft band X-ray image is superposed with the LOFAR contours. The limited resolution of the radio images however do not allow us to detect the corresponding inner lobes/jets.

From the central panel of Fig. 4, we can also notice that all the radio emission is confined to the surrounding cocoon. The high energy associated with the outburst has displaced and compressed the material in the cluster atmosphere, creating a confining shell that hinders the advance of any radio plasma.

We also checked if there is more diffuse emission, re-imaging the LOFAR data at lower resolution. The overall morphology of the source in that case is consistent with what has

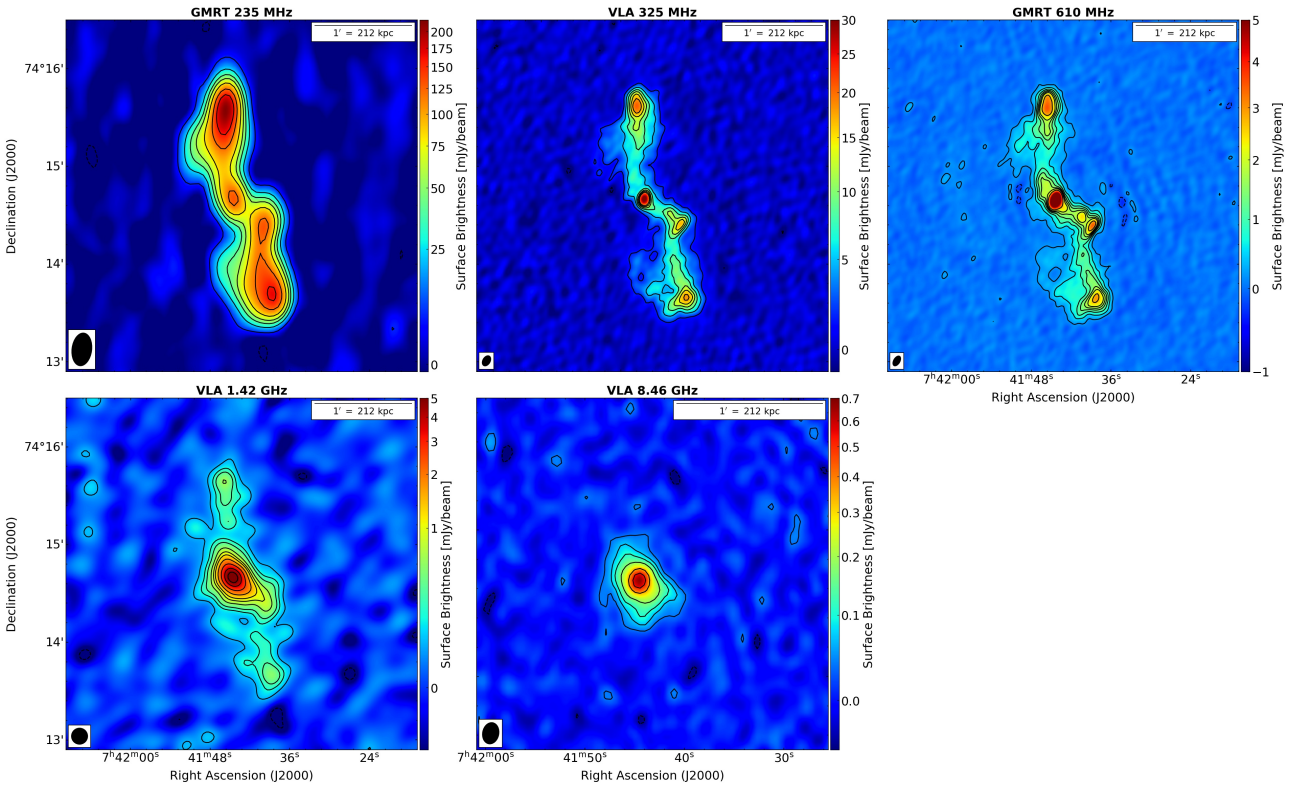

Fig. 3: Radio maps of MS0735 at different frequencies. *Top Left*: GMRT 235 MHz at $20'' \times 12''$ resolution. Levels: $[-1, 1, 3, 5, 7, 10, 15, 20, 30] \times 3\sigma$ (where $\sigma = 2.7$ mJy beam^{-1}). *Top Middle*: VLA 325 MHz image at $7'' \times 5''$ resolution. Levels: $[-1, 1, 3, 5, 7, 9, 11, 15, 20] \times 3\sigma$ ($\sigma = 0.53$ mJy beam^{-1}). *Top Right*: GMRT 610 MHz at $7'' \times 4''$ resolution. Levels: $[-1, 1, 3, 5, 7, 9, 11, 15, 18, 30, 50] \times 3\sigma$ ($\sigma = 6.0 \times 10^{-2}$ mJy beam^{-1}). *Bottom Left*: VLA 1420 MHz at $10'' \times 10''$ resolution. Levels: $[-1, 1, 2, 3, 5, 7, 9, 13, 20, 30, 40] \times 3\sigma$ ($\sigma = 4.2 \times 10^{-2}$ mJy beam^{-1}). *Bottom right*: VLA 8460 MHz at $9'' \times 7''$ resolution. Levels: $[-1, 1, 2, 3, 5, 10, 15] \times 3\sigma$ ($\sigma = 1.18 \times 10^{-2}$ mJy beam^{-1}). The beam is shown in the bottom left corner of each image.

Table 3: Cavity properties.

Cavity	a [kpc]	b [kpc]	R [kpc]	E_{cav} [10^{59} erg]	t_{buoy} [Myr]	t_{c_s} [Myr]	t_{ref} [Myr]	$P_{cav,buoy}$ [10^{44} erg s^{-1}]
Northern outer	109 ± 16	106 ± 16	150	440 ± 200	91	120	240	160 ± 70
Southern outer	120 ± 15	100 ± 21	186	440 ± 200	110	140	250	130 ± 60
Intermediate	48 ± 9	42 ± 7	85 - 100	23 - 60	62 - 64	53 - 69	103 - 120	12 - 30
Northern inner	13.3 ± 1.6	10.1 ± 2.3	19.3	3.6 ± 2.0	33	19	74	3.6 ± 2.0
Southern inner	15.5 ± 2.2	10.5 ± 3.3	25.0	3.6 ± 2.4	41	25	78	2.9 ± 2.0

Notes. For each cavity: semi-minor axis (a), semi-major axis (b), distance from cluster center (R), energy of the cavity (E_{cav}), buoyancy time-scale (t_{buoy}), sound crossing time-scale (t_{c_s}) refilling time-scale (t_{ref}) and power of the cavity ($P_{cav,buoy} = E_{cav}/t_{buoy}$). The values for the outer and inner cavities are taken from Table 2 of Vantyghem et al. (2014).

been previously observed at 325 MHz (Cohen et al. 2005). While the radio lobes are more extended at 144 MHz, we find no evidence of any older outbursts.

In Fig. 3, we show images of MS0735 at different frequencies, made from the archival data described earlier. Moving to higher frequencies, the morphology of the source changes: the central region (which includes the core and the inner jets) becomes dominant while the lobes become less prominent, until they are no longer visible at 8460 MHz. To check if this variation is real or due to different observational setups, we re-imaged all the datasets using the same *uv*-range, with a `uniform` weighting scheme, and convolving all images to the same resolution (see Low resolution column of Table 4). Even in this case the morphological differences remain, indicating that the lack of lobe emission at 8460 MHz is really due to the spectral steepening rather than to instrumental effects. This implies a sharp cut-off in the spectrum of the outer lobes, typical of aged plasma.

Considering the morphology at different frequencies, MS0735 may overcome the boundaries of the Fanaroff-Riley classification (Fanaroff & Riley 1974), in that it could be either at different points of the activity cycle. The outer lobes exhibit the classical morphology of FRII radio galaxies, with lobes and hotspots (visible also in the VLA and GMRT images up to 1420 MHz). The second phase of activity may have created another FRII, presenting an increase in brightness in the Intermediate lobe, but at 610 MHz the jets are clearly visible, which is un-

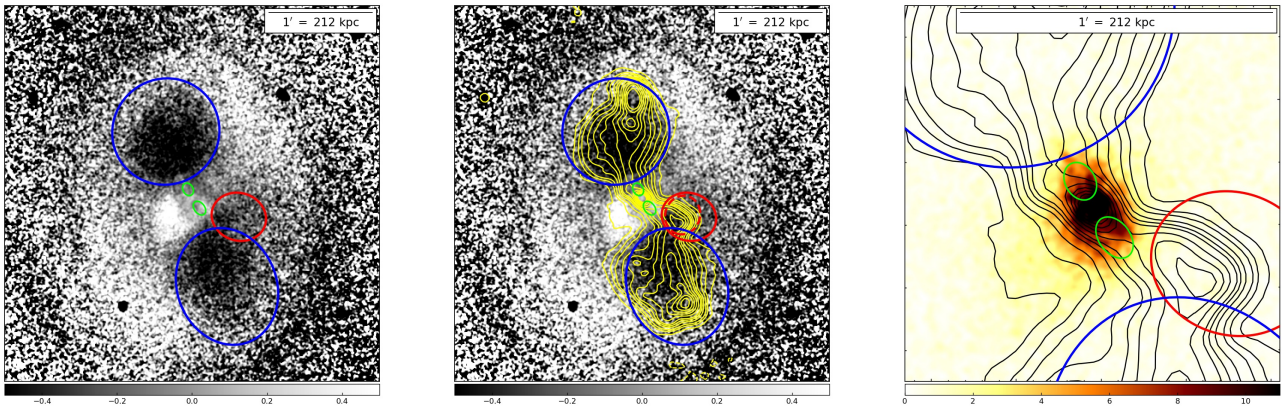

Fig. 4: *Chandra* images of MS0735. *Left:* Residual image after subtracting a double−β model from the X-ray image (0.5−7 keV). The image is in units of counts pixel^{-1} and is Gaussian-smoothed with a 1 arcsec kernel radius. The dark regions to the north and south correspond to two large cavities, marked by blue ellipses. A surface brightness edge surrounds these cavities and corresponds to a weak shock front. Red ellipse marks the newly discovered intermediate cavity south-west of the core, while green ellipses show the inner cavities. *Middle:* same as before with superposed LOFAR contours at 144 MHz and the smaller region outlined by the red dashed ellipse is considered to place a lower limit on the size of the intermediate cavity. *Right:* soft band (0.3−1.0 keV) image in units of counts pixel^{-1}, Gaussian-smoothed with a 1 arcsec kernel radius. Two regions of low surface brightness, interpreted as a pair of cavities originating from a recent AGN outburst are indicated with green ellipses. Superposed are the LOFAR contours at 144 MHz and the blue and red ellipses showing the outer and intermediate cavities, respectively.

usual for this class of source. It is therefore possible that the source was born as an FRII, and was then slowed down by the dense surrounding medium at the center of the cool-core cluster. In this scenario, the source could have turned into an FRI-type radio galaxy during subsequent phases of jet activity (e.g. Laing 1994; Kaiser & Best 2007; Meliani et al. 2008; Wang et al. 2011; Turner & Shabala 2015; Kapińska et al. 2017).

Understanding the nature of the source and its variation throughout its life is beyond the scope of this paper. For our purposes, that is estimating the radiative life of the outer lobes and of the Intermediate lobe, we will assume that the source is an FRII, so the particle acceleration took place in the hotspots. In the following sections, we will discuss this point further.

3.2. X-ray features

Vantyghem et al. (2014) detected the presence of two large cavities, with diameter of ∼ 200 kpc and a shock front enveloping the cavities, both clearly visible in the left and middle panels of Fig. 4. The projected sizes and positions of the cavities were determined by eye by approximating the surface brightness depressions with elliptical regions, see blue ellipses in Fig. 4. The northern cavity is best represented by an ellipse with semi-major axis a = 109±16 kpc, semi-minor axis b = 106±16 kpc, and projected distance from the AGN, R = 150 kpc. The southern cavity is best represented by an ellipse with a = 120 ± 15, b = 100 ± 21, and R = 186 kpc. The cocoon shock front is approximated by an ellipse with semi-major axis a = 320 kpc and semi-minor axis b = 230 kpc.

The deep *Chandra* image in the soft band (0.3 - 1.0 keV), right panel of Fig. 4, revealed two smaller cavities located along the radio jets in the inner 20 kpc. Their positions and sizes are shown in all the panels of Fig. 4 with green ellipses. These cavities are best represented by an ellipse with a = 13.3 ± 1.6 kpc, b = 10.1 ± 2.3 kpc and projected distance of R = 19.3 kpc from cluster center for the inner northern cavity and a = 15.5 ± 2.2, b = 10.5 ± 3.3 and R = 25.0 kpc for the inner southern cavity.

We performed a further visual inspection of the X-ray residual image which led to the possible detection of an additional cavity, located to the south-west of the core at an intermediate distance from the cluster center with respect to that of the two cavities reported in Vantyghem et al. (2014). No corresponding cavity to the north-east of the core has been detected. This newly-identified cavity (referred to as the intermediate cavity), represented with a red ellipse in Fig. 4, is distinct from the region used for the analysis of the outer cavity to the south (Vantyghem et al. 2014), represented with a blue ellipse. Since the radio emission is less sensitive to projection effects than depressions in the X-ray image, we considered different dimensions for the intermediate cavity (as done, e.g. in Gitti et al. 2010), ranging from the size of the apparent depression seen in the residual X-ray image (red solid ellipse) to the extension of the Intermediate radio lobe (red dashed ellipse in middle panel of Fig. 4). Our analysis provides a range of values for the semi-major axis a = 39 - 56 kpc, the semi-minor axis b = 35 - 48 kpc and the distance from the cluster center R = 85 - 100 kpc.

We estimated the energetics and age of this newly-detected intermediate cavity following the same procedure used by Vantyghem et al. (2014) for the other cavities. The minimum total energy required to create a cavity, for a relativistic gas, is $E_{\rm cav} = 4pV$, where p is the cavity pressure and V is its volume. Assuming pressure equilibrium, the pressure is estimated from the deprojected pressure profile of the surrounding ICM (Fig. 7 of Vantyghem et al. 2014) at a radius corresponding to the distance of the cavity centre. The cavity volume is calculated using the geometric mean between oblate and prolate ellipsoids, $V = 4/3\pi(ab)^{3/2}$. The age of the cavity is estimated using three characteristic time-scales: the sound crossing time, buoyancy time, and refill time (e.g. Bîrzan et al. 2004). At the distance of the intermediate cavity, we estimated a sound velocity of $c_s = 1210-1260$ km s^{-1}. The gravitational acceleration, g, used to calculate the buoyancy and refill time-scales was determined using the MS0735 mass profile from Hogan et al. (2017). Finally, we estimate the power required to inflate the cavity, as $P_{\rm cav} = 4pV/t_{\rm buoy}$, where we use the buoyancy time-scale as ref-

Table 4: Summary of imaging parameters.

Parameter	High resolution	Low resolution
Frequency range	144 - 1420 MHz	144 - 1420 MHz
	(excluding 235 MHz)	(all)
Restoring beam	$6.5'' \times 6.5''$	$16'' \times 10''$, PA 0°
uv-range	$157 \sim 19173\ \lambda$	$157 \sim 40186\ \lambda$
Weighting	`uniform`	`uniform`

erence for the cavity age. The properties and energetics of the intermediate cavity derived in this work, along with those of the inner and outer cavities studied by Vantyghem et al. (2014), are reported in Table 3.

Therefore, X-ray data have revealed that there were at least three AGN outbursts in MS0735. For now, only few sources with multiple cavities are known, for example Hydra A (Nulsen et al. 2005; Wise et al. 2007; Gitti et al. 2011) and NGC 5813 (Randall et al. 2011, 2015). The presence of different episodes of jet activity is important to ensure the continuous heating of the central gas and so to prevent its cooling.

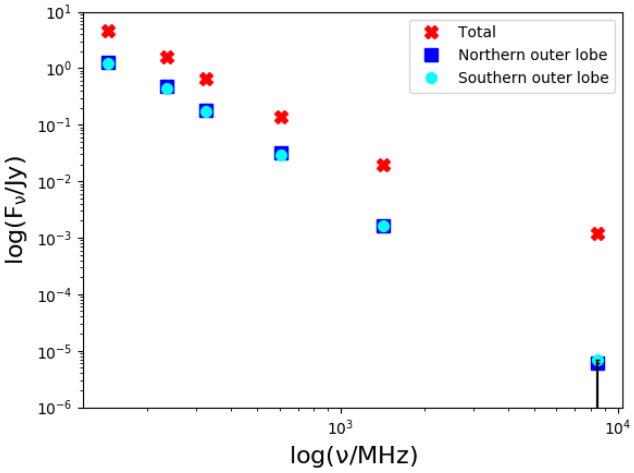

Fig. 5: Total flux density distribution of MS0735 between 144 MHz and 1420 MHz (in red) and of the northern and southern outer lobes (in blue and cyan, respectively). We have also set a 3σ upper limit for the flux of the lobes at 8460 MHz, since they are not detected.

3.3. Radio spectral study

To perform a spectral study of the source we re-imaged all the radio data with the same restoring beam ($16'' \times 10''$, PA 0°), *uv*-range ($157 \sim 19173\ \lambda$) and using a `uniform` weighting scheme. We exclude the data at 8460 MHz, where the emission of the lobes is not visible. Finally, we spatially align all the images, to correct for possible shifts introduced by the phase self-calibration process, using only the central compact emission as reference, since there are no visible point sources in the vicinity of the target. After this procedure the spatial difference between the images is reduced to less than 0.1 pixel.

Furthermore, for a more detailed study of the central regions of the source, we create another set of images at higher resolution, excluding the GMRT data at 235 MHz. The exclusion of this frequency has a minimal impact on the results of the study since it lies between two points at frequencies very close to each other. These high resolution images have a restoring beam of $6.5''$. The parameters of the two sets of images are listed in Table 4.

From the images at lower resolution, we measure the total flux density of the source and of the outer lobes, reported in Table 5 and plotted in Fig. 5. We also put an upper limit for the lobes emission at 8460 MHz, estimated as the product between the rms noise at 8460 MHz and the lobe area expressed in units of beams ($3\sigma \times N_{\rm beam}$).

We use the Broadband Radio Astronomy Tools (`BRATS`)[1] software package (Harwood et al. 2013, 2015) to estimate the spectral age of the source. BRATS allows one to perform a detailed spectral analysis, on a pixel-by-pixel basis. In this way, we can map the source properties (e.g. spectral index, spectral age) throughout the source extension. The detection limit was set to three times the noise, estimated as the rms in an empty region in the field.

3.3.1. Spectral index maps

To investigate the spatial distribution of the spectral index, we have made a high-resolution ($6.5''$) two-frequency spectral index map using LOFAR 144 MHz and GMRT 610 MHz images (see left panel Fig. 6). To our knowledge, this is the first time that a spectral index study of MS0735 extended to this low frequency is presented at high resolution.

Previous work, based on integrated spectra, have found an ultra-steep radio spectrum for this source ($\alpha_{325}^{1425} = 2.45 \pm 0.04$ Cohen et al. 2005, $\alpha_{327}^{1400} = 2.48 \pm 0.04$ Bîrzan et al. 2008). Our resolved spectral study confirms that this trend extends to 144 MHz, with spectral index values reaching $\alpha_{144}^{610} = 3.1 \pm 0.3$. Curiously, the spectrum remains very steep even at the location of the core, where the spectral index is $\alpha_{144}^{610} = 1.5 \pm 0.1$, as previously observed at higher frequency ($\alpha_{325}^{1425} = 1.54 \pm 0.04$, Cohen et al. 2005). This steep value suggests that we are observing a superposition of the core and the lobes emission. The emission from the central region will be further analysed in the next section.

In addition, we note a gradient of the spectral index along the main axis of the source. Starting from a value of $\alpha_{144}^{610} = 2.3 \pm 0.1$ in the hotspots, at the edges of the outer lobes, it steepens going towards the core, reaching a maximum value of $\alpha_{144}^{610} = 2.9 \pm 0.3$ in the outer lobes, then it flattens again in the central regions and in the Intermediate lobe, where the spectral index is $\alpha_{144}^{610} = 2.1 \pm 0.1$. This trend suggests the presence of two different episodes of jet activity. In fact, if there was only one phase of jet activity, we would expect a gradual increase in the spectral index going from the hotspot, where the particles are last accelerated, to the core where there are the oldest particles. Instead, in the central regions the spectral index is flatter than in the outer lobes, indicating the presence of younger particles, which were therefore emitted later. Such ultra-steep spectral indices in hotspots occur in $\leq 0.5\%$ of cases (Hogan et al. 2015). This likely indicates that the acceleration of particles is not active anymore in these regions, otherwise we would expect a spectral index in the range 0.6-0.8, as observed for typical FRII-type radio galaxies (Jaffe & Perola 1973; Carilli et al. 1991; Komissarov & Gubanov 1994).

In the middle and right panels of Fig. 6, we show respectively the low-frequency spectral index map between 144 MHz and 235 MHz and the high-frequency spectral index map between 610 MHz and 1420 MHz, both at the resolution of $16'' \times 10''$.

[1] http://www.askanastronomer.co.uk/brats/

Table 5: Total flux density of MS0735 and of the outer lobes.

Telescope	ν [MHz]	Total [Jy]	Northern outer lobe [Jy]	Southern outer lobe [Jy]
LOFAR	144	4.7 ± 0.5	1.3 ± 0.1	1.2 ± 0.1
GMRT	235	1.6 ± 0.2	$(4.8 \pm 0.5) \times 10^{-1}$	$(4.4 \pm 0.4) \times 10^{-1}$
VLA	325	$(6.5 \pm 0.3) \times 10^{-1}$	$(1.8 \pm 0.1) \times 10^{-1}$	$(1.8 \pm 0.1) \times 10^{-1}$
GMRT	610	$(1.4 \pm 0.1) \times 10^{-1}$	$(3.1 \pm 0.3) \times 10^{-2}$	$(3.0 \pm 0.3) \times 10^{-2}$
VLA	1420	$(2.0 \pm 0.2) \times 10^{-2}$	$(1.7 \pm 0.1) \times 10^{-3}$	$(1.6 \pm 0.1) \times 10^{-3}$
VLA	8460	$(1.20 \pm 0.03) \times 10^{-3}$	$(\sim 6.1 \times 10^{-6})$	$(\sim 6.9 \times 10^{-6})$

Notes. 3σ upper limit are shown at 8460 MHz for the lobes flux density, since they are not detected.

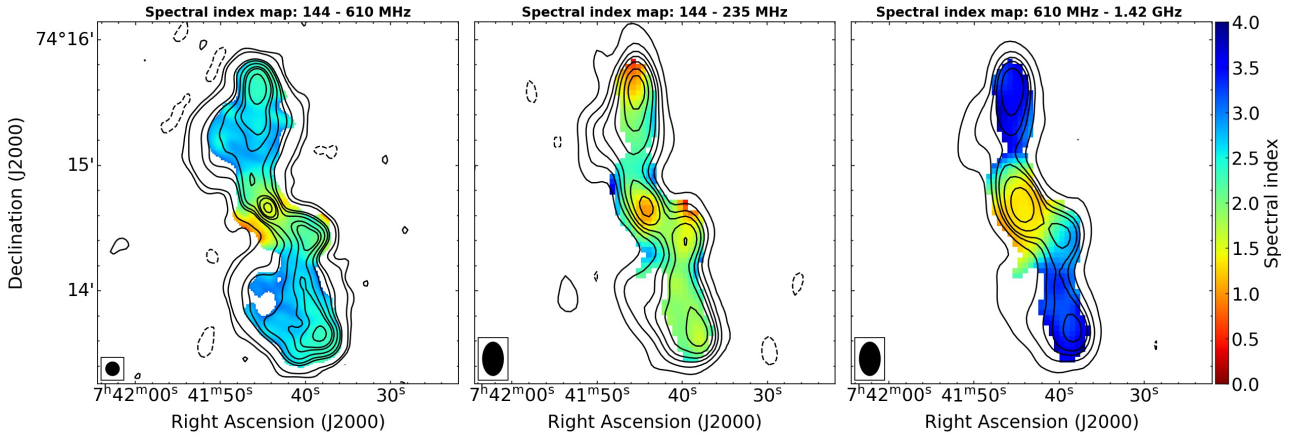

Fig. 6: *Left:* High resolution spectral index map between 144 MHz and 610 MHz, resolution = 6.5″. Overlaid are the LOFAR contours. *Middle:* Low frequency spectral index map between 144 MHz and 235 MHz, res = 16″ × 10″. Overlaid are the 235 MHz contours. *Right:* High frequency spectral index map between 610 MHz and 1420 MHz, resolution = 16″ × 10″. Overlaid are the 610 MHz contours. The beam is shown in the bottom left corner of each map.

Narrowing the frequency range between 144 and 235 MHz, the spectrum is less steep than that represented in the map obtained between 144 and 610 MHz. This is especially true in the hotspot of the northern outer lobe where the spectral index reaches the minimum value of $\alpha_{144}^{235} = 0.75 \pm 0.4$, much closer to typical values. The hotspot in the southern outer lobe is instead less pronounced and has a steeper spectral index, $\alpha_{144}^{235} = 1.6 \pm 0.4$. This difference may be due to projection effects in the southern outer lobe, with an overlap along the line of sight of particles of different ages, making the spectrum steeper. At higher frequencies, instead, the spectrum is very steep and we recover the values found by Cohen et al. (2005) for the center and the outer lobes. For the main features of the source, we list in Table 6 the average spectral index at low and high frequencies and their difference, which represents the spectral curvature of these regions (SPC = $\alpha_{\rm high} - \alpha_{\rm low}$). For both the outer lobes and the Intermediate lobe, the high-frequency spectral index is steeper than that observed at low frequency, and, despite the large uncertainties, the spectral curvature is high, indicating emission from an aged population of electrons.

Table 6: Spectral indices ($\alpha_{\rm low}$, $\alpha_{\rm high}$) and spectral curvature (SPC) for main features of MS0735.

Region	$\alpha_{\rm low}$	$\alpha_{\rm high}$	SPC
Center	1.2±0.4	1.4±0.1	0.2±0.5
Northern outer lobe	2.1±0.4	3.4±0.6	1.3±0.9
Northern hotspot	0.75±0.4	3.4±0.6	2.6±0.9
Southern outer lobe	2.0±0.4	3.4±0.6	1.4±0.9
Southern hotspot	1.6±0.4	3.4±0.6	1.8±0.9
Intermediate lobe	1.5±0.4	2.8±0.3	1.3±0.7

3.3.2. The central emission

As explained above, the central region of MS0735 exhibits a steep radio spectrum, with $\alpha = 1.5 \pm 0.1$ between 144−610 MHz, which is much steeper than typical AGN cores. However, we note that at the resolution of 6.5″ ≅ 23 kpc, the actual core is likely not resolved, and the observed emission (and thus apparent steep spectrum) could result from the superposition of different populations of electrons from the inner jets/lobes. The detection of inner cavities in fact demonstrates that there has been a more recent jet activity (Vantyghem et al. 2014).

To investigate this region further, we have analysed high resolution archival VLA observations of the source. These observations (at 1420 MHz array A and 8460 MHz array A, listed in Sect. 2.2) were performed without the use of short baselines, so the diffuse emission is filtered out, allowing us to study the real compact emission of the nuclear region.

In Fig. 7, we show the radio map of the central emission at 1420 MHz (left panel), at 3.1″ × 1.1″ resolution, at 8460 MHz

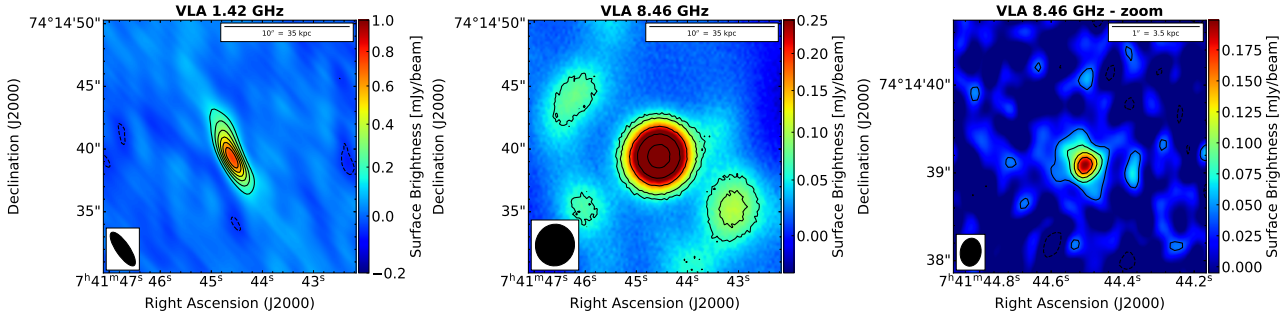

Fig. 7: Radio maps of the central emission of MS0735. *Left*: VLA 1420 MHz at 3.1″ × 1.1″. Levels: [−1, 3, 5, 7, 9, 11, 13] ×3σ (σ = 17 μJy beam^{-1}). *Middle*: VLA 8460 MHz at 3.3″ × 3.1″ resolution. Levels: [−1, 1, 1.5, 3, 5, 8] ×3σ (σ = 20 μJy beam^{-1}). *Right*: zoom of VLA 8460 MHz at 0.32″ × 0.24″ resolution. Levels: [−1, 1, 2, 3, 4] ×3σ (σ = 13 μJy beam^{-1}). The beam is shown in the bottom left corner of each image.

(middle panel) 3.3″ × 3.1″ resolution, and the emission at 8460 MHz (right panel), at 0.32″ × 0.24″ resolution.

To measure the flux densities of the central emission component at 1420 MHz and 8460 MHz, we used images produced with a common uv-range (17926 ∼ 353657 λ) and a resolution of 2″ ≅ 7 kpc.

We obtain a spectral index of 0.75 ± 0.08 for this central component. This supports the idea that, even at this resolution, the emission we observe is not purely core emission — which would have a much flatter spectrum (e.g. Blandford & Königl 1979; Hogan et al. 2015) — but rather a superposition of emission from the core and the inner part of the jets.

3.3.3. Radiative age

For a synchrotron-emitting electron population, initially distributed along a power-law, the energy loss rate scales as $E/(dE/dt) \propto 1/E$. This leads to a faster cooling of high energy electrons and, in absence of further particle acceleration, produces a spectrum, initially described by a power-law, which becomes increasingly curved over time. A break in the spectrum develops at frequency ν_b, which relates to the time elapsed since the injection and to the magnetic field as $\nu_b \propto B^{-3}t^{-2}$. Therefore, if we know the magnetic field strength, we can derive the age of a radio source from the shape of its spectrum.

A modern approach to derive the spectral age of the source consists of fitting the observed radio spectrum with a modelled spectrum that is obtained by numerical integration of the equations that describe the radiative losses of the plasma. BRATS follows this approach and allows one to fit the observed radio spectrum with different spectral ageing models, obtaining a spectral age map of the source. On small scales, particles can be likely assumed as part of a single injection event.

Three single-injection models are usually considered: the JP (Jaffe & Perola 1973), KP (Kardashev 1962; Pacholczyk 1970) and Tribble (Tribble 1993) models. JP and KP models consider synchrotron and inverse-Compton losses in a constant magnetic field environment, where the radio emitting electron population has a fixed pitch angle (in the KP model) or a continuously isotropized pitch angle distribution (in the JP model).

The JP model is more realistic from a physical point of view, as an anisotropic pitch angle distribution will become more isotropic due to scattering.

The Tribble model is a more complex model which attempts to account for a spatially non-uniform magnetic field by integrating the standard JP losses over a Maxwell–Boltzmann magnetic field distribution. The model implemented in the BRATS code is a specific version, that is the low field, high diffusion case (Harwood et al. 2013; Hardcastle 2013).

Major differences between the models are visible at frequencies higher than the break frequency (ν_b), while at lower frequencies all models are expected to have a spectral index equal to the injection index (α_{inj}), which describes the initial distribution of the electron population.

We have tested all the models and found that the final numbers are consistent within 10%. Therefore, we report here, for simplicity, only the results obtained fitting the Tribble model which, as tested on other sources in the literature (e.g. Harwood et al. 2013), provides both a good fit to observations as well as providing a more physically realistic description of the source.

We fit the models over a range of injection indices, and found that the lowest chi-squared value is obtained with α_{inj} = 1.5. This injection index is much steeper than classical values (between 0.5 and 0.7, see e.g. Jaffe & Perola 1973; Carilli et al. 1991; Komissarov & Gubanov 1994), and is not physically explainable with current particle acceleration models. It is also steeper than the highest value found up to now, 1.2 for the cluster-center radio galaxy 3C28 (Harwood et al. 2015), whose physical interpretation has been attributed to the jet terminating in a weak shock. However, the injection index can also be constrained by the low-frequency spectrum of the regions where particles are accelerated, that is in the hotspots or jets if the source is an FRII or FRI, respectively. Indeed, the MHz-frequency part of the spectrum is the last affected by the ageing and can preserve information on the shape of the original energy distribution of the injected particles. We therefore used for our modelling an injection index of 0.75, which is the lowest spectral index value found in the hotspot of the northern outer lobe in the frequency range 144-325 MHz and is also consistent with values from the literature recently found from resolved spectral studies of FRII radio galaxies (0.75−0.85; Harwood et al. 2013, 2015, 2017b; Shulevski et al. 2017). For completeness, we report in Appendix A the results obtained with the well-fitting injection index value of 1.5.

To derive the magnetic field in the outer lobes, we made the assumption of equipartition between particles and magnetic field, using the following parameters:

– We have assumed a power-law particle distribution of the form $N(\gamma) \propto \gamma^{-\delta}$ between a minimum and maximum Lorentz

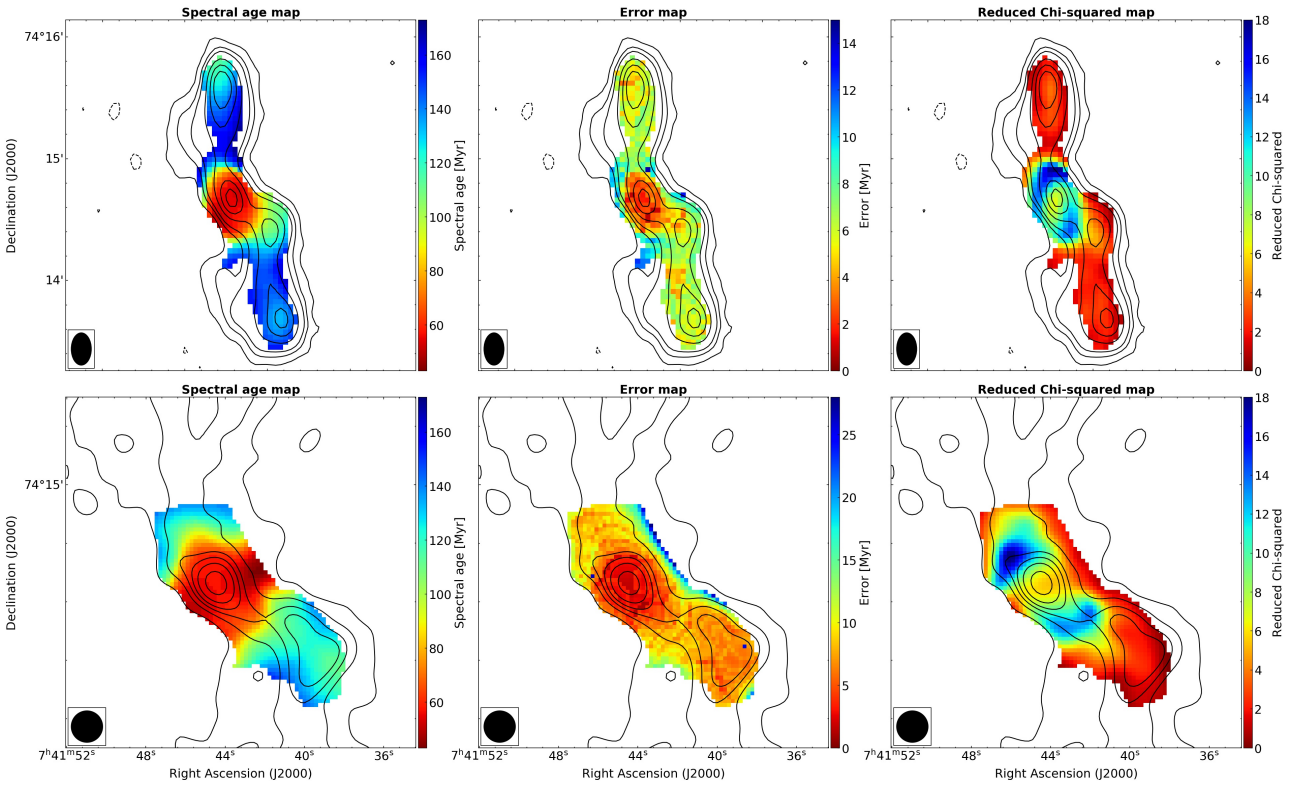

Fig. 8: Tribble spectral ageing maps (*left*) and corresponding error maps (*middle*) and reduced Chi-squared maps (*right*) of the entire source at a resolution of 16″ × 10″ (*top panels*) and of the central regions at a higher resolution of 6.5″ (*bottom panels*). Overlaid are the 325 MHz contours. For the fit we set $\alpha_{\rm inj} = 0.75$ and $B_{\rm eq} = 5.9$ μG.

factor of $\gamma_{\rm min} = 100$ and $\gamma_{\rm max} = 10^7$ (Falcke & Biermann 1995; Reynolds et al. 1996; Dunn et al. 2006). The particle energy power-law index (δ) is related to the injection index by $\delta = 2\alpha_{\rm inj} + 1$.

– The particle energy is equally divided between electrons and protons, setting $k = E_{\rm p}/E_{\rm e} = 1$.
– We derived the flux density and the volume of the lobes at the LOFAR frequency, approximating the lobes geometry to a prolate ellipsoid with $V = \frac{4\pi}{3}ab^2$, where a and b are respectively the semi-major and semi-minor axes. For the northern lobe $a = 31.5''$ and $b = 24.6''$, while for the southern lobe $a = 27''$ and $b = 26''$. The total flux of the lobes at 144 MHz is 3.3 Jy.

For $\alpha_{\rm inj} = 0.75$, we derive a magnetic field strength of $B_{\rm eq} \sim 5.9$ μG, in agreement with the equipartition magnetic field of 4.7 μG derived by Bîrzan et al. (2008).

To derive the age of the Intermediate lobe we use the values of the injection index and magnetic field derived for the outer lobes, and we repeat the fit on the high resolution images of the source. In Fig. 8, we show the spectral age map, error map and chi-squared map of the whole source (*upper panels*) and of the high resolution zoom on the central regions (*bottom panels*). The results of the fit are reported in Table 7, while in Fig. 9 one representative spectral plot of a well-fitted single region in the southern outer lobe is shown for the purpose of illustration.

We can reconstruct the first phase of jet activity from the ages obtained in the outer lobes. The maximum age found in the lobes represents the total age of the source, while the minimum age represents the OFF time, that is the time elapsed since the last particle acceleration in the outer lobes. Consequently, we can estimate the duration of the first active phase (ON time) as

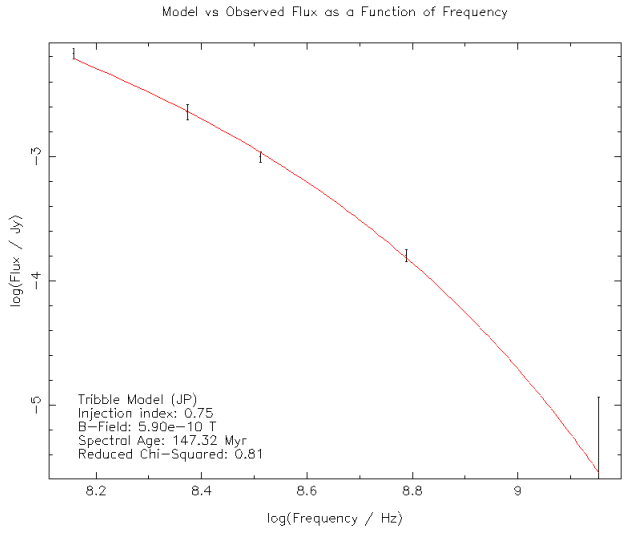

Fig. 9: Flux density distribution of an example region in the southern outer lobe, fitted with the Tribble model, setting $\alpha_{\rm inj} = 0.75$ and $B_{\rm eq} = 5.9$ μG.

the difference between the oldest and the youngest age found in the outer lobes: $t_{\rm ON} = t_{\rm max} - t_{\rm min}$, following the approach in Shulevski et al. (2017) and Brienza et al. (2020). The total age, OFF age and ON age for the northern and southern outer lobes are reported in Table 7.

To estimate the spectral age of the Intermediate lobe we refer to the high resolution spectral age map shown in the bottom

panels of Fig. 8. However, in this region there is only a slight age gradient from the hotspot towards the center, which is not significant enough to obtain robust values for the maximum and minimum age, due to both resolution and the presence of different components (southern outer lobe, Intermediate lobe and central emission). Therefore we can only give an estimate of the duration of the second phase of jet activity, without distinguishing between the active and off time.

To complete the spectral age study of MS0735, we also considered a second category of models that assumes a continuous injection of particles: the continuous injection (CI) and the so-called CIoff models (Pacholczyk 1970; Komissarov & Gubanov 1994). With respect to single injection models, in the CI models the source is fuelled at a constant rate by the nuclear activity for a duration t_{ON} (the 'continuous injection phase'). In this phase the radio spectrum presents a first break frequency which depends on the total age of the source t_{tot}:

$$\nu'_{break} \propto \frac{B}{(B^2 + B^2_{CMB})^2 t^2_{tot}} \quad (1)$$

where $B_{CMB} = 3.18(1+z)^2$ is the inverse Compton equivalent magnetic field. Below and above ν'_{break} the spectral indices are respectively α_{inj} and $\alpha_{inj} + 0.5$.

While in the CI model the source is continuously fuelled by fresh particles, in the CIoff, at the time t_{ON}, the power supply of the nucleus is switched-off and a new phase of duration t_{OFF} begins (the 'dying phase'). A new break frequency then appears, beyond which the radiation spectrum drops precipitously:

$$\nu''_{break} = \nu'_{break}\left(\frac{t_{tot}}{t_{OFF}}\right)^2 \quad (2)$$

with $t_{tot} = t_{ON} + t_{OFF}$. Thus, the CIoff model is described by four parameters: the injection index, the two break frequencies and the normalization. As in the JP model, the synchrotron and inverse-Compton losses are modelled using a continuously isotropized pitch angle.

These models are applicable only if the injected particles are confined to the fitted regions, so we can fit them only to the integrated flux of selected regions, shown in Fig. 10.

We selected different sub-regions within the 'Center + Intermediate lobe' region depicted in Fig. 10, in order to determine whether the Intermediate lobe is still being fuelled by the jet. The integrated flux densities for these regions are presented in Fig. 11. Our results suggest that each sub-region within the inner part of MS0735 is well-described by a single power-law fit, with a slope of $\alpha = 1.5$ for the Center, $\alpha = 2.23$ for the Intermediate lobe and $\alpha = 1.79$ for Center + Intermediate lobe, showing no evidence of a spectral break. This could be explained by ongoing injection of particles, or alternatively through the superposition of various components from different phases. Hence, we can not estimate the spectral ages from the integrated flux densities of these regions.

Conversely, the outer lobes exhibit curved spectra, indicating aged emission, which is consistent with the lack of detection at 8460 MHz (see bottom right panel of Fig. 3). We fit the spectra of the outer lobes using the CI and CIoff models, fixing the injection index to the same values used for the resolved spectral study ($\alpha_{inj} = 0.75$ and 1.5). For both outer lobes we find that the CI model does not provide a good fit to the data, while the CIoff model provides a better fit. The particle supply in the outer lobes is expected to have switched off, as both the radio and X-ray data

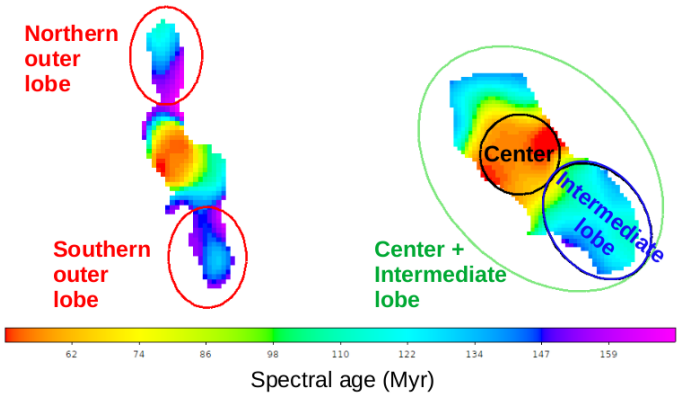

Fig. 10: Representation of the regions used to measure the integrated flux density of the main features of the source, selected based on their age. The flux density of the outer lobes is measured from the low resolution images, while we used the higher resolution images to measure the flux of the Center and of the Intermediate lobe.

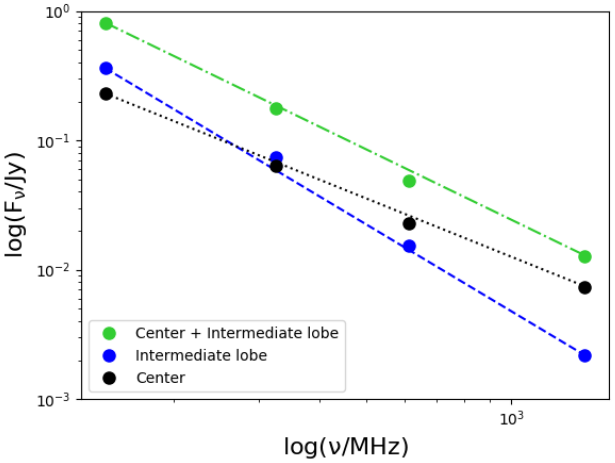

Fig. 11: Integrated flux density as a function of frequency for the central regions shown in Fig. 10. The Center region is represented with the black dotted line; the Intermediate lobe with the blue dashed line, and the total flux of these regions with the green dash-dotted line. In all the cases, the spectra show no evidence of curvature and/or spectral breaks; they are well-described by a power-law with a slope of $\alpha = 1.5$ for the Center, $\alpha = 2.23$ for the Intermediate lobe and $\alpha = 1.79$ for Center + Intermediate lobe. The size of the points represents the dimension of the flux density error.

revealed the presence of subsequent phases of jet activity. Furthermore, similar to the Tribble model discussed before, the best fit of the CIoff model is obtained with $\alpha_{inj} = 1.5$ (see Appendix A for the results of the fit).

The CIoff model fitting results with $\alpha_{inj} = 0.75$ are reported in Table 7, while the fit of the northern outer lobe flux density is shown in Fig. 12. We note that the reduced chi-squared of this fit ($\chi^2_{red} = 4.71$) is greater than that obtained from the single-region Tribble model fit ($\chi^2_{red} = 2.66$), shown in Fig. 9. This is true for all the regions in the outer lobes, as is visible from the map in the top right panel of Fig. 8, where the reduced chi-squared value is always lower than 4.

Table 7: Tribble & CIoff fitting results and correction for adiabatic expansion.

		$\alpha_{\rm inj} = 0.75$			$B_{\rm eq} = 5.9\,\mu$G						
		Tribble model					CIoff model				
Region	Age	$\nu_{\rm break}$ [MHz]	t [Myr]	$\nu^{\rm corr}_{\rm break}$ [MHz]	$t^{\rm corr}$ [Myr]	$\chi^2_{\rm red}$	$\nu_{\rm break}$ [MHz]	t [Myr]	$\nu^{\rm corr}_{\rm break}$ [MHz]	$t^{\rm corr}$ [Myr]	$\chi^2_{\rm red}$
Northern outer lobe	Tot	159	170 ± 6	413	106 ± 4	1.04	13.6	475 ± 200	0.8	2369 ± 800	4.71
	Off	347	115 ± 7	902	71 ± 4	1.95	466	81 ± 1	28	405 ± 4	–
	On	–	55 ± 15	–	35 ± 8	–	–	394 ± 201	–	1964 ± 804	–
Southern outer lobe	Tot	166	163 ± 7	481	98 ± 4	1.09	10.2	548 ± 200	0.6	2770 ± 800	5.68
	Off	259	133 ± 6	751	78 ± 4	2.52	473	80 ± 1	28	405 ± 4	–
	On	–	30 ± 15	–	20 ± 8	–	–	468 ± 201	–	2365 ± 804	–
Intermediate lobe	Tot	308	122 ± 7	431	103 ± 6	2.60	–	–	–	–	–

Notes. The break frequency ($\nu_{\rm break}$) and the synchrotron age (t) derived from the fitting model, the adiabatic-loss corrected break frequency ($\nu^{\rm corr}_{\rm break}$) and synchrotron age ($t^{\rm corr}$) and finally the reduced chi-squared of the fit ($\chi^2_{\rm red}$). Those parameters are derived for both the total age (Tot), the dying phase (Off) and the active phase (On) of the lobes using two different models (Tribble and CIoff), setting $\alpha_{\rm inj} = 0.75$ and $B_{\rm eq} = 5.9\,\mu$G.

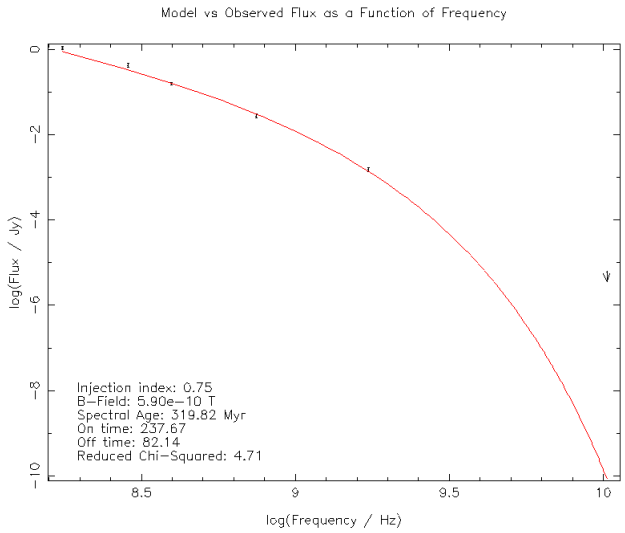

Fig. 12: Results of the CIoff model fit on the northern outer lobe, using $\alpha_{\rm inj} = 0.75$.

As shown in Table 7, our $\alpha_{\rm inj} = 0.75$ fit provides a very low first break frequency ($\nu_{\rm break} \sim 10 - 15$ MHz), which falls outside the frequency range sampled by our observations. The associated total age of the source ($t \sim 0.5$ Gyr) is therefore very high. Even considering the high uncertainties for this value, the discrepancy with the maximum age derived in the resolved spectral study is very large.

3.4. Adiabatic losses correction

The spectral ages derived in the previous section assume that particles only undergo synchrotron and inverse-Compton energy losses. However, previous X-ray observations have indicated that the cavities filled by the outer lobes were created by low-density bubbles of radio plasma, inflated by the jet, which have displaced the surrounding gas rising buoyantly and expanding adiabatically. Hence, adiabatic losses should be taken into account.

The effect of adiabatic losses is to reduce the particle energy and the magnetic field in radio lobes (Scheuer & Williams 1968). The shape of the synchrotron spectrum is preserved, but it is shifted towards lower (or higher) frequencies, if there is a single (or continuous) injection of particles (Kardashev 1962; Murgia et al. 1999). The radiative ages estimated from standard models of spectral ageing without considering the adiabatic expansion exceed (or underestimate) the true age of the source if the synchrotron-emitting electrons are generated in a short-term (or continuous injection) event.

The radiative ages estimated in the previous section can be corrected by multiplying the break frequency with a corrective factor F:

$$\nu^{corr}_{\rm break} = \nu^{obs}_{\rm break} \times F, \tag{3}$$

where, for a single injection of particles:

$$F = \left(\frac{\Delta^{2n} - 1}{2n}\right)^2, \tag{4}$$

while, for a continuous injection of particles:

$$F = \frac{1}{4n^2}. \tag{5}$$

Here, Δ is the linear expansion factor for a volume of plasma and n is the exponent of the magnetic field variation $B(t) = B_0\Delta^{-n} = B_0(t/t_0)^{-n}$. We set $n = 2$, assuming the magnetic flux is conserved during the expansion.

Following the procedure of Bîrzan et al. (2008), we calculated Δ as the ratio between the final radius of the bubble at the end of the adiabatic expansion (r_1) and the initial radius of the bubble at the start of the adiabatic expansion (r_0), which we assumed to be the cluster center. According to the adiabatic expansion law:

$$\Delta = \frac{r_1}{r_0} = \left(\frac{p_1}{p_0}\right)^{-1/3\gamma}, \tag{6}$$

where the ratio of specific heats γ, is assumed to be 4/3, p_1 is the gas pressure at the location of the X-ray cavity and $p_0 = 5.4\times10^{-10}$ erg/cm^3 is the gas pressure at the center of the cluster (derived from X-ray observations; see Vantyghem et al. 2014, and Sect. 3.2). For the intermediate lobe the detected pressure is less reliable due to the uncertainty about the cavity size and the scatter in the density profile at that distance.

The assumption that the particles are all injected at the central pressure and expand to the current X-ray pressure at each

Table 8: Adiabatic losses corrective factors.

Region	p_1 [erg cm^{-3}]	Δ	$F_{\rm Tribble}$	$F_{\rm CIoff}$
Northern outer lobe	7.3×10^{-11}	1.65	2.6	0.06
Southern outer lobe	6.9×10^{-11}	1.67	2.9	0.06
Intermediate lobe	9.5×10^{-11}	1.54	1.4	0.06

lobe position likely overestimates the adiabatic correction, which is generally modest. This is especially true in our case, as the source is at the center of a cool-core cluster, where the gas pressure is high enough to confine the lobes. Hence, the lobes remain luminous for longer time with respect to remnant lobes in more rarefied environments.

In Table 8, we list the pressure at the location of the intermediate and outer cavities (p_1), the linear expansion factor (Δ) and the corrective factors ($F_{\rm Tribble}$ and $F_{\rm CIoff}$) for both the outer lobes and the Intermediate lobe. The corrected break frequencies and ages are reported in Table 7.

4. Discussion

In this work we have studied the peculiar radio source at the centre of the cool-core cluster MS0735. A detailed study of the source in the radio band, together with a re-inspection of the X-ray data, revealed that the source was subjected to at least three different phases of jet activity. From the radio spectrum we have derived estimates of the radiative age of the source under different hypotheses, in order to reconstruct its duty cycle and to provide an independent comparison with previously-established age estimates from the cavities detected in X-rays. We also aimed to estimate the power of the jet, to confirm whether the energy released in the ICM during the jet activity is enough to stop the cooling flow, and to verify if the bubbles are in pressure equilibrium with the surrounding medium.

4.1. Spectral ages and duty cycle

A first attempt to derive the spectral age of the source MS0735 was performed by Bîrzan et al. (2008). Since data at only two frequencies were available at the time, it was not possible to derive the break frequency from the integrated spectra of the outer lobes. So the spectral age was estimated using the relation of Myers & Spangler (1985), assuming $\alpha_{\rm inj} = 0.5$. The frequency coverage and high resolution of the data presented in this work allow us to reconstruct the radiative history of the source.

The source MS0735 has experienced throughout its life at least three different episodes of jet activity.

The outer lobes, the best known regions of this source, match perfectly with the outer cavities and represent the first phase of jet activity visible today. These regions present a very steep and curved spectrum, indicating that particle injection has finished. We can therefore give an estimate of their age and reconstruct the duty cycle of the first phase of jet activity. From the spectral ageing modelling of the northern outer lobe spectrum we derived that the first outburst started around $t_{\rm tot} = 170 \pm 6$ Myr ago and it lasted about $t_{\rm ON} = 55 \pm 15$ Myr before to switch-off ($t_{\rm OFF} = 115 \pm 7$ Myr). Similar values are found from the southern outer lobe (see Table 7). These numbers are obtained assuming only the presence of synchrotron and inverse-Compton losses, neglecting the adiabatic losses due to the bubble expansion. Therefore the ages reported above could be considered as an upper limit for the true radiative age of the source. The age values of the northern outer lobe corrected for adiabatic losses are: $t_{\rm tot} = 106 \pm 3$ Myr, $t_{\rm OFF} = 71 \pm 3$ Myr and $t_{\rm ON} = 35 \pm 6$ Myr (see Sect. 3.4). These have been obtained using an upper limit for the lobes expansion and can therefore been considered as a lower limit to the actual lobe age. In summary, the total age of the outer lobes lies in the range 106 Myr $\lesssim t_{\rm tot} \lesssim$ 170 Myr and the first phase of jet activity lasted around 35 Myr $\lesssim t_{\rm ON} \lesssim$ 55 Myr.

The second phase of jet activity is associated with the Intermediate lobe, which also presents an overall steep spectrum, and fills the new discovered intermediate cavity. The age gradient in this region cannot be well constrained due to the available resolution. Therefore, we only provide an estimated of the start of the second phase of jet activity, which lies in the range 103 Myr $\lesssim t_{\rm tot} \lesssim$ 122 Myr, depending on the contribution of the adiabatic expansion. We note that these values are comparable with the age of the outer lobes, indicating that jet activity has been immediately reactivated, with an inactivity time around few and ten Myr.

The third phase of the jet activity is represented by the inner lobes, for which, however, we are not able to give an estimate of the age, as they are not resolved. Indeed, the central regions of the source are poorly described by the Tribble model, as indicated by the high chi-squared values obtained (lower right panel of Fig. 8), resulting from the likely superposition of particles emitted at different times. However, the measurement at high resolution of a central spectral index of 0.75 suggests the presence of active jets on scales of some kpc. Furthermore, the detection of inner cavities on the same scale ensures the reactivation of jet activity. The age of the inner cavities could then be used to give a constrain on the duration of the second phase. Considering the age of the southern inner cavity (25−78 Myr, depending on the scenario, Vantyghem et al. 2014) and that of the Intermediate lobe, the jet cannot be active for more than $t_{\rm ON} \leq 44 - 78$ Myr.

Overall our new analysis suggests that the source is going through a very rapid cycle where most of the time the central AGN is active and there are only brief quiescent phases. The presence of several close episodes of jet activity ensures a continuous source of heating to the central gas, preventing its cooling.

We remind the reader that our discussion on the source age and duty cycle is based on the results of the resolved spectral study, which we consider more reliable. Indeed the analysis performed on the integrated spectrum has provided less certain results. The total times derived from the fit of the CIoff model are three times higher than those derived from the resolved study, and so unrealistic. Furthermore, the chi-squared values of the CIoff fit on the integrated spectra of the outer lobes are higher compared to those obtained from the Tribble model fit on single regions. As shown in Harwood (2017a), a discrepancy between the spectral ages derived from integrated and resolved analysis is not surprising. Indeed, an integrated study is not able to provide good constraints with respect to the model parameters. Furthermore, the goodness-of-fit is highly dependent on frequency coverage, if the spectrum is not well constrained around the spectral break, as is our case for the first break frequency.

When compared with other radio galaxies the time-scales we observe MS0735 are in accordance with the typical activity time, between tens and hundreds Myr, and inactivity time, between few and tens Myr (e.g. Konar et al. 2013; Orrù et al. 2015; Shulevski et al. 2017; Brienza et al. 2018, 2020; Maccagni et al. 2020). Unfortunately there are not many similar studies on radio galaxies at the center of clusters to make a direct comparison. The only ones are 3C438, 3C28 (Harwood et al. 2015), which

Table 9: Radio lobe vs X-ray cavity age estimates.

Region	t_{rad} [Myr]	$t_{buoyancy}$ [Myr]	t_{Cs} [Myr]	t_{refill} [Myr]
Northern outer lobe/ Northern outer cavity	106−170	91	120	240
Southern outer lobe/ Southern outer cavity	98−163	110	140	250
Intermediate lobe/ Intermediate cavity	103−122	62-64	53-69	103-120

Notes. For the age of the radio lobe (t_{rad}) derived from our analysis we report a range of values, with the highest derived with a simple radiative Tribble model fit, while the lowest one is corrected for adiabatic losses. The three X-ray cavity age estimates are based on the buoyancy time-scale ($t_{buoyancy}$), the sound crossing time-scale (t_{Cs}) and the refill time-scale (t_{refill}). The southern and northern outer cavity time-scales are derived by Vantyghem et al. (2014), while we estimate the time-scales for the Intermediate cavity reporting a range of values for the different dimensions of the cavity considered.

present a single phase of jet activity and are younger (maximum age in the lobes of ∼ 4 and ∼ 17 Myr respectively) and 3C388 (Brienza et al. 2020), which instead is a restarted source with a total age of 82 Myr and a longer activity time than the quiescent period, as seen in our source. However, the sample is not large enough to draw general conclusions.

4.2. Comparison with X-ray estimates

An independent estimate of the source age was made by Vantyghem et al. (2014) from the X-ray data, providing different time-scales for the formation of the outer cavities. We can then compare the total radiative age we derived for the outer lobes with the age derived from X-rays for the corresponding cavities. To our knowledge there are no studies of sources in clusters in which this type of comparison has been made, it was only performed for a source in a galaxy group (Kolokythas et al. 2020), so it is important to understand whether the two estimates are consistent, as they found, or not.

Three different time-scales are used to derive the age of the cavities: the buoyancy, sound crossing, and refill time-scale. In general, the ages calculated using the speed of sound are the shortest, those based on the refilling time-scale are the longest, and the buoyancy time-scale — based on the terminal velocity of the bubbles — lies in-between. However, in the case of the outer cavities of MS0735, the terminal velocity is supersonic, so the buoyancy time-scale is the shortest. Neglecting the bubble's expansion history in the buoyancy time-scale therefore underestimates the true cavity age. All time-scales are reported in Table 9.

When comparing the age estimates of the outer lobes/cavities, we notice that the buoyancy (91 Myr) and sound crossing time-scales (120 Myr) are comparable with the derived range of radiative ages (106−170 Myr), while the refilling time-scale (240 Myr) is much larger. We note that from the X-ray analysis it appears that the refilling time-scale is overestimated, since it is higher than the age of the surrounding shock front (t_{shock} = 110 Myr), which should be comparable to the true cavity age (Vantyghem et al. 2014). We then suggest that the refilling scenario is the least reliable.

A comparison can also be made for the age of the Intermediate lobe/cavity. We follow the procedure used by Vantyghem et al. (2014) to compute the three different time-scales for this new cavity, reported in Table 9. Conversely to the outer lobes, the range of radiative ages that we found for this lobe (103−122 Myr) is comparable to the estimates provided by the refilling scenario.

For the inner cavities, on the other hand, we cannot make comparable statements as we have not been able to estimate the age of the radio emission on the same scale.

Overall, we note that the two ways of estimating the age of a source give consistent results. When the radiative age is better constrained, this allows to reduce the number of methods to calculate the age of the cavity. However, our results are not sufficient to determine which is the most realistic.

4.3. Energetics

In this section we estimate the energetics of the source, starting from the radio properties of the outer lobes. Deriving the total power of the source is important to understand if the gas heating by AGN is enough to quench the cooling flow in the cluster center, as observed from the X-rays. X-ray analysis of this source has revealed that the energy released by the AGN outburst (∼ 8×10^{61} erg) is enough to quench a cooling flow for several Gyr (McNamara et al. 2005; Gitti et al. 2007; Vantyghem et al. 2014). If we take the mean of the buoyancy time-scales of the outer cavities ($t \sim 100$ Myr) as an estimate of the cavity age, the mechanical power required to inflate the bubbles is of $P = E/t = 1.4 \times 10^{46}$ erg s^{-1}. The same estimate can be performed based on the radio data presented in this work as follows.

It is not easy to estimate the total power of the source, because there are different components that contribute to it. First of all, we can compute the total radio luminosity for the outer lobes by integrating the flux between the rest-frame frequencies of 10 and 10000 MHz as

$$L_{rad} = \frac{4\pi D_L^2 S_{\nu_0}}{(1+z)^{(1-\alpha)}} \int_{\nu_1}^{\nu_2} (\nu/\nu_0)^{-\alpha} d\nu, \quad (7)$$

where we used the flux density measured at 144 MHz as the flux reference (S_{ν_0}), and set the spectral index to $\alpha = 2.9$. This is the value derived in the outer lobes, using our data at 144 MHz and 610 MHz (since this spectral index is probably measured above the break frequency, integrating to low frequency will overestimate the luminosity). We obtain a total radio luminosity of $L_{rad} = 7 \times 10^{43}$ erg s^{-1}.

The energy dissipated into synchrotron radiation is only a minor fraction of the jet power. The bulk of the jet power is converted into energizing the lobes, which contain both relativistic particles and a magnetic field. The total energy is hence given by the sum of these contributions $E_{tot} = (1 + k)E_e + E_B$, where k is the ratio between the energy of protons and electrons, which we have set equal to one. Both the particle and the magnetic field energy depend on the magnetic field strength, which is difficult to

measure, so an estimate can be derived by invoking minimum-energy arguments. The condition of minimum energy approximately corresponds to energy equipartition between particles and magnetic field. For the equipartition magnetic field strength derived in Sect. 3.3.3, $B_{eq} \sim 5.9$ μG, the minimum energy contained in the lobes is $E_{min} \sim 9 \times 10^{59}$ erg. Furthermore, we can use our estimate of the lobe age to determine the average jet power over the lifetime of MS0735.

Using the total age of northern outer lobe ($t_{tot} = 62 - 170$ Myr), we derive a range for the power $P_{jet} \sim 2-5\times10^{44}$ erg s^{-1}, which is two orders of magnitude lower than the power derived from the X-rays and comparable with the X-ray bolometric luminosity within the cooling radius (2.6×10^{44} erg s^{-1}), balancing radiative losses. However, we must consider that in our calculation we used the minimum energy inside the lobes, so the power actually injected could be larger. Furthermore, neither estimate accounts for the power emitted to drive shocks into the external medium, as observed from X-ray data.

From the minimum energy we can also estimate the minimum pressure inside the lobes, the sum of the contribution of the magnetic field and of the plasma (for a relativistic plasma $p = U/3$, where U is the energy density). This yields $p \sim 2\times10^{-12}$ erg cm^{-3}, which is again two orders of magnitude lower than the gas pressure of the external medium derived from the X-rays ($\sim 2 \times 10^{-10}$ erg cm^{-3}). This is clearly unphysical, as in such a case the bubbles would collapse under the pressure of the external medium.

In our estimates we have considered that the particle energy is equally divided between electrons and protons (k=1) and that the lobes are completely filled with radio plasma (filling factor $\phi = 1$). To reach pressure equilibrium, keeping the equipartition principle valid, we can decrease the filling factor and increase the contribution of the protons. In this case we would assume $k \geq 2000$ and $\phi \leq 30\%$, generating much higher magnetic field strengths ($B_{eq} \sim 60\,\mu$G) and therefore unrealistic short plasma ages (~ 3 Myr). Furthermore, the strongest evidence that this is not the case is given by the fact that FRII radio galaxies have light jets (Hardcastle et al. 2002; Croston et al. 2004, 2005, 2018). Therefore, either equipartition does not apply in the outer lobes of MS0735 or there is additional pressure support (e.g. from entraining of hot thermal gas).

In the case of FRII sources, where it was possible to directly measure the magnetic field strength from observations of inverse-Compton emission, it has been shown that typical magnetic field strength is a factor 2-3 below equipartition values (e.g. Croston et al. 2005; Kataoka & Stawarz 2005; Migliori et al. 2007; Ineson et al. 2017; Turner et al. 2018), suggesting that the lobes contain electron energy densities larger than what implied by the minimum energy condition. Accordingly, the total energy would be higher than the minimum energy by a factor on average around 2. However, departure from equipartition is not sufficient to provide the solution to the underpressured lobes of MS0735.

In conclusion, an additional pressure support is required to keep bubbles in equilibrium. This could be provided by hot thermal gas entrained by the jet, as proposed to compensate for the large pressure disparity observed in few other sources, for example the intermediate FRI/FRII source Hydra A (Croston & Hardcastle 2014) and the FRII source 3C438 (Harwood et al. 2015). To entrain material, a jet must move slowly, but that of FRII sources is supposed to remain relativistic up to great distances. However, MS0735 does not show the typical morphology of an FRII, as already noted, so a slow moving jet could provide a solution to both the pressure gap and its atypical morphology.

5. Conclusions

In this paper, we have presented new LOFAR observations of the source MS 0735.6+7421. These data, combined with archival GMRT and VLA data at higher frequencies, allowed us to perform a resolved spectral study of this source, expanding previous work both in frequency range and in resolution. The main results are summarised below:

- Our new LOFAR data show two giant outer radio lobes, much wider than at higher frequencies, with a hotspot at the extremity. These lobes perfectly fill the X-ray outer cavities. There is also evidence of an Intermediate lobe south of the core, confirmed by our discovery of a corresponding cavity, after a re-inspection of the X-ray data. Therefore, the source experienced a further phase of jet activity, in addition to the two already known from previous analysis of X-ray data.
- Previous work have pointed out the presence of a steep spectrum for this source. Our work confirms this result. The spectrum is steep down to 144 MHz both in the outer lobes ($\alpha^{610}_{144} \sim 2.9$) and in the more central regions ($\alpha^{610}_{144} \sim 2.1$). Additionally, the hotspots in the outer lobes show a steep spectral index ($\alpha^{610}_{144} \sim 2.4$), indicating that the particle acceleration mechanisms in these regions has ceased to operate. However, the spectral index flattens at low frequencies to a value of $\alpha^{235}_{144} \sim 0.75$.
- Our high resolution images of the central emission at 1420 MHz and 8460 MHz show a spectral index of $\alpha^{8460}_{1420} = 0.75 \pm 0.08$. This suggest that within the central component the actual AGN core and the inner active jets are blended.
- We used single-injection models to estimate the radiative age of the radio lobes and found a total age for the outer lobes in the range 106-170 Myr and for the Intermediate lobe in the range 103-122 Myr, depending on the effect of adiabatic losses. We compare radiative ages with X-ray estimates from cavity time-scales. The age range of the outer lobes we found is in good agreement with buoyancy and sound crossing time-scales derived from X-rays (Vantyghem et al. 2014).
- We reconstruct the duty cycle of the source, finding that the first phase of jet activity lasted for around $t_{ON} = 35 - 55$ Myr and we put an upper limit on the duration of the second phase ($t_{ON} \leq 44 - 78$ Myr). The two episodes are separated by a brief quiescent phase of few Myr. The source, therefore, has a duty cycle close to unity, with the AGN being active for most of the time.
- By comparing the pressure estimates inside the cavities, derived from the minimum total energy and from the thermal gas, we found that additional pressure support, for instance from entraining of hot thermal gas, is necessary to maintain the bubbles.

We have demonstrated the importance of performing a resolved spectral study to reconstruct the duty cycle of a radio source, necessary to understand the AGN feedback. With the high resolution and sensitivity reached with the new generation of radio telescopes (LOFAR, the Karl G. Jansky VLA, the uGMRT and in the near future with the advent of the Square Kilometre Array; SKA), resolved spectral studies will be enabled on an increasing number of sources, allowing us to perform the first statistical studies of these objects, as well as shedding new light on the history of very well-known sources such as MS0735.

Acknowledgements

We thank the Referee for helpful comments. NB, MB, AB, EB, CJR acknowledge support from the ERC through the grant ERC-Stg DRANOEL n. 714245. ACE acknowledges support from STFC grant ST/P00541/1. LOFAR, the Low Frequency Array designed and constructed by ASTRON (Netherlands Institute for Radio Astronomy), has facilities in several countries, that are owned by various parties (each with their own funding sources), and that are collectively operated by the International LOFAR Telescope (ILT) foundation under a joint scientific policy. The scientific results reported in this article are based in part on data obtained from the VLA Data Archive, the GMRT Data Archive and the *Chandra* Data Archive. This research made use of different packages for pyhton: APLpy (Robitaille & Bressert 2012), Astropy (Astropy Collaboration et al. 2013), NumPy (van der Walt et al. 2011) and SciPy (Virtanen et al. 2020).

References

Astropy Collaboration, Robitaille, T. P., Tollerud, E. J., et al. 2013, A&A, 558, A33
Bîrzan, L., McNamara, B. R., Nulsen, P. E. J., Carilli, C. L., & Wise, M. W. 2008, ApJ, 686, 859
Bîrzan, L., Rafferty, D. A., McNamara, B. R., Wise, M. W., & Nulsen, P. E. J. 2004, ApJ, 607, 800
Blandford, R. D. & Königl, A. 1979, ApJ, 232, 34
Brienza, M., Morganti, R., Harwood, J., et al. 2020, A&A, 638, A29
Brienza, M., Morganti, R., Murgia, M., et al. 2018, A&A, 618, A45
Carilli, C. L., Perley, R. A., Dreher, J. W., & Leahy, J. P. 1991, ApJ, 383, 554
Chandra, P., Ray, A., & Bhatnagar, S. 2004, ApJ, 612, 974
Cohen, A. S., Clarke, T. E., Feretti, L., & Kassim, N. E. 2005, ApJ, 620, L5
Croston, J. H., Birkinshaw, M., Hardcastle, M. J., & Worrall, D. M. 2004, MNRAS, 353, 879
Croston, J. H. & Hardcastle, M. J. 2014, MNRAS, 438, 3310
Croston, J. H., Hardcastle, M. J., Harris, D. E., et al. 2005, ApJ, 626, 733
Croston, J. H., Ineson, J., & Hardcastle, M. J. 2018, MNRAS, 476, 1614
De Young, D. S. 1984, Phys. Rep., 111, 373
de Young, D. S. 2002, The physics of extragalactic radio sources
Donahue, M. & Stocke, J. T. 1995, ApJ, 449, 554
Donahue, M., Stocke, J. T., & Gioia, I. M. 1992, ApJ, 385, 49
Doria, A., Gitti, M., Ettori, S., et al. 2012, ApJ, 753, 47
Dunn, R. J. H., Fabian, A. C., & Celotti, A. 2006, MNRAS, 372, 1741
Fabian, A. C. 1994, ARA&A, 32, 277
Fabian, A. C., Sanders, J. S., Ettori, S., et al. 2000, MNRAS, 318, L65
Falcke, H. & Biermann, P. L. 1995, A&A, 293, 665
Fanaroff, B. L. & Riley, J. M. 1974, MNRAS, 167, 31P
Forman, W. & Jones, C. 1982, ARA&A, 20, 547
Giacintucci, S., Markevitch, M., Johnston-Hollitt, M., et al. 2020, ApJ, 891, 1
Gitti, M., Feretti, L., & Schindler, S. 2006, A&A, 448, 853
Gitti, M., McNamara, B. R., Nulsen, P. E. J., & Wise, M. W. 2007, ApJ, 660, 1118
Gitti, M., Nulsen, P. E. J., David, L. P., McNamara, B. R., & Wise, M. W. 2011, ApJ, 732, 13
Gitti, M., O'Sullivan, E., Giacintucci, S., et al. 2010, ApJ, 714, 758
Hardcastle, M. J. 2013, MNRAS, 433, 3364
Hardcastle, M. J., Alexander, P., Pooley, G. G., & Riley, J. M. 1998, MNRAS, 296, 445
Hardcastle, M. J., Birkinshaw, M., Cameron, R. A., et al. 2002, ApJ, 581, 948
Hardcastle, M. J. & Croston, J. H. 2020, arXiv e-prints, arXiv:2003.06137
Hardcastle, M. J., Shimwell, T. W., Tasse, C., et al. 2020, arXiv e-prints, arXiv:2011.08294
Harwood, J. J. 2017a, MNRAS, 466, 2888
Harwood, J. J., Hardcastle, M. J., & Croston, J. H. 2015, MNRAS, 454, 3403
Harwood, J. J., Hardcastle, M. J., Croston, J. H., & Goodger, J. L. 2013, MNRAS, 435, 3353
Harwood, J. J., Hardcastle, M. J., Morganti, R., et al. 2017b, MNRAS, 469, 639
Heald, G. H., Pizzo, R. F., Orrú, E., et al. 2015, A&A, 582, A123
Hogan, M. T., Edge, A. C., Hlavacek-Larrondo, J., et al. 2015, MNRAS, 453, 1201
Hogan, M. T., McNamara, B. R., Pulido, F. A., et al. 2017, ApJ, 851, 66
Ineson, J., Croston, J. H., Hardcastle, M. J., & Mingo, B. 2017, MNRAS, 467, 1586
Intema, H. T. 2014, in Astronomical Society of India Conference Series, Vol. 13, Astronomical Society of India Conference Series, 469
Intema, H. T., Jagannathan, P., Mooley, K. P., & Frail, D. A. 2017, A&A, 598, A78
Jaffe, W. J. & Perola, G. C. 1973, A&A, 26, 423
Kaiser, C. R. & Best, P. N. 2007, MNRAS, 381, 1548
Kapińska, A. D., Terentev, I., Wong, O. I., et al. 2017, AJ, 154, 253
Kardashev, N. S. 1962, Soviet Ast., 6, 317
Kataoka, J. & Stawarz, Ł. 2005, ApJ, 622, 797
Kellermann, K. I. & Owen, F. N. 1988, Radio galaxies and quasars., ed. K. I. Kellermann & G. L. Verschuur, 563–602
Kokotanekov, G., Wise, M., Heald, G. H., et al. 2017, A&A, 605, A48
Kolokythas, K., O'Sullivan, E., Giacintucci, S., et al. 2020, MNRAS, 496, 1471
Komissarov, S. S. & Gubanov, A. G. 1994, A&A, 285, 27
Konar, C., Hardcastle, M. J., Jamrozy, M., & Croston, J. H. 2013, MNRAS, 430, 2137
Laing, R. A. 1994, in Astronomical Society of the Pacific Conference Series, Vol. 54, The Physics of Active Galaxies, ed. G. V. Bicknell, M. A. Dopita, & P. J. Quinn, 227
Maccagni, F. M., Murgia, M., Serra, P., et al. 2020, A&A, 634, A9
McMullin, J. P., Waters, B., Schiebel, D., Young, W., & Golap, K. 2007, in Astronomical Society of the Pacific Conference Series, Vol. 376, Astronomical Data Analysis Software and Systems XVI, ed. R. A. Shaw, F. Hill, & D. J. Bell, 127
McNamara, B. R., Kazemzadeh, F., Rafferty, D. A., et al. 2009, ApJ, 698, 594
McNamara, B. R. & Nulsen, P. E. J. 2007, ARA&A, 45, 117
McNamara, B. R. & Nulsen, P. E. J. 2012, New Journal of Physics, 14, 055023
McNamara, B. R., Nulsen, P. E. J., Wise, M. W., et al. 2005, Nature, 433, 45
McNamara, B. R., Wise, M., Nulsen, P. E. J., et al. 2000, ApJ, 534, L135
Meliani, Z., Keppens, R., & Giacomazzo, B. 2008, A&A, 491, 321
Migliori, G., Grandi, P., Palumbo, G. G. C., Brunetti, G., & Stanghellini, C. 2007, ApJ, 668, 203
Mitchell, R. J., Culhane, J. L., Davison, P. J. N., & Ives, J. C. 1976, MNRAS, 175, 29P
Morganti, R. 2017, Nature Astronomy, 1, 596
Murgia, M., Fanti, C., Fanti, R., et al. 1999, A&A, 345, 769
Myers, S. T. & Spangler, S. R. 1985, ApJ, 291, 52
Nulsen, P. E. J., McNamara, B. R., Wise, M. W., & David, L. P. 2005, ApJ, 628, 629
Offringa, A. R., McKinley, B., Hurley-Walker, N., et al. 2014, MNRAS, 444, 606
Orr, M. J. L. & Browne, I. W. A. 1982, MNRAS, 200, 1067
Orrù, E., van Velzen, S., Pizzo, R. F., et al. 2015, A&A, 584, A112
Pacholczyk, A. G. 1970, Radio astrophysics. Nonthermal processes in galactic and extragalactic sources
Perley, R. A. & Butler, B. J. 2013, ApJS, 204, 19
Peterson, J. R. & Fabian, A. C. 2006, Phys. Rep., 427, 1
Peterson, J. R., Kahn, S. M., Paerels, F. B. S., et al. 2003, ApJ, 590, 207
Randall, S. W., Forman, W. R., Giacintucci, S., et al. 2011, ApJ, 726, 86
Randall, S. W., Nulsen, P. E. J., Jones, C., et al. 2015, ApJ, 805, 112
Reynolds, C. S., Fabian, A. C., Celotti, A., & Rees, M. J. 1996, MNRAS, 283, 873
Robitaille, T. & Bressert, E. 2012, APLpy: Astronomical Plotting Library in Python
Scaife, A. M. M. & Heald, G. H. 2012, MNRAS, 423, L30
Scheuer, P. A. G. & Williams, P. J. S. 1968, ARA&A, 6, 321
Serlemitsos, P. J., Smith, B. W., Boldt, E. A., Holt, S. S., & Swank, J. H. 1977, ApJ, 211, L63
Shimwell, T. W., Röttgering, H. J. A., Best, P. N., et al. 2017, A&A, 598, A104
Shimwell, T. W., Tasse, C., Hardcastle, M. J., et al. 2019, A&A, 622, A1
Shulevski, A., Morganti, R., Harwood, J. J., et al. 2017, A&A, 600, A65
Smirnov, O. M. & Tasse, C. 2015, MNRAS, 449, 2668
Swarup, G. 1990, Indian Journal of Radio and Space Physics, 19, 493
Tadhunter, C. 2016, A&A Rev., 24, 10
Tasse, C. 2014a, arXiv e-prints
Tasse, C. 2014b, A&A
Tasse, C., Hugo, B., Mirmont, M., et al. 2018, A&A, 611, A87
Tribble, P. C. 1993, MNRAS, 261, 57
Turner, R. J. & Shabala, S. S. 2015, ApJ, 806, 59
Turner, R. J., Shabala, S. S., & Krause, M. G. H. 2018, MNRAS, 474, 3361
van der Walt, S., Colbert, S. C., & Varoquaux, G. 2011, Computing in Science and Engineering, 13, 22
van Diepen, G., Dijkema, T. J., & Offringa, A. 2018, DPPP: Default Pre-Processing Pipeline
van Haarlem, M. P., Wise, M. W., Gunst, A. W., et al. 2013, A&A, 556, A2
van Weeren, R. J., de Gasperin, F., Akamatsu, H., et al. 2019, Space Sci. Rev., 215, 16
Vantyghem, A. N., McNamara, B. R., Russell, H. R., et al. 2014, MNRAS, 442, 3192
Virtanen, P., Gommers, R., Oliphant, T. E., et al. 2020, Nature Methods, 17, 261
Wang, Y., Knigge, C., Croston, J. H., & Pavlovski, G. 2011, MNRAS, 418, 1138
Wise, M. W., McNamara, B. R., Nulsen, P. E. J., Houck, J. C., & David, L. P. 2007, ApJ, 659, 1153

Appendix A: $\alpha_{\rm inj} = 1.5$

We report the fitting results obtained setting the injection index to $\alpha_{\rm inj} = 1.5$, which gives the lowest chi-squared value to the models fit. The results of the fit computed for both the Tribble and CIoff models, together with the ages corrected for the presence of adiabatic losses, are summarised in Table A.1.

Table A.1: Tribble & CIoff fitting results and correction for adiabatic expansion.

$\alpha_{\rm inj} = 1.5$ $B_{\rm eq} = 15\ \mu$G											
		Tribble model					CIoff model				
Region	Age	$\nu_{\rm break}$ [MHz]	t [Myr]	$\nu^{\rm corr}_{\rm break}$ [MHz]	$t^{\rm corr}$ [Myr]	$\chi^2_{\rm red}$ [MHz]	$\nu_{\rm break}$ [Myr]	t [MHz]	$\nu^{\rm corr}_{\rm break}$ [Myr]	$t^{\rm corr}$	$\chi^2_{\rm red}$
Northern outer lobe	Tot	358	42 ± 3	931	26 ± 2	0.48	188	47 ± 7	11	238 ± 28	1.11
	Off	1170	19 ± 2	3042	14 ± 1	3.43	1160	19 ± 1	70	94 ± 4	–
	On	–	23 ± 5	–	12 ± 3	–	–	28 ± 8	–	144 ± 32	–
Southern outer lobe	Tot	424	38 ± 2	1230	22 ± 1	0.35	153	52 ± 13	9	263 ± 52	0.73
	Off	741	29 ± 2	2149	17 ± 1	0.97	1240	18 ± 1	74	92 ± 4	–
	On	–	9 ± 4	–	5 ± 2	–	–	34 ± 14	–	171 ± 56	–
Intermediate lobe	Tot	743	30 ± 2	1040	24 ± 2	0.72	–	–	–	–	–

Notes. The break frequency ($\nu_{\rm break}$) and the synchrotron age (t) derived from the fitting model, the adiabatic-loss corrected break frequency ($\nu^{\rm corr}_{\rm break}$) and synchrotron age ($t^{\rm corr}$) and finally the reduced chi-squared of the fit ($\chi^2_{\rm red}$). Those parameters are derived for both the total age (Tot), the dying phase (Off) and the active phase (On) of the lobes using two different models (Tribble and CIoff), setting $\alpha_{\rm inj} = 1.5$ and $B_{\rm eq} = 15\ \mu G$).